UNIVERSITY OF CALIFORNIA,
IRVINE

Accounting for Motion Artifact and Optical Property Changes in Laser Speckle Imaging

DISSERTATION

submitted in partial satisfaction of the requirements
for the degree of

DOCTOR OF PHILOSOPHY

in Biomedical Engineering

by

Ben Srun Lertsakdadet

Dissertation Committee:
Professor Bernard Choi, Chair
Professor Gultekin Gulsen
Doctor Mustafa Kabeer

2019

DEDICATION

To all my friends, mentors, and family that have kept my spirit high through the lows

To my parents for their never-ending love and support

To Eileen for her patience and understanding

TABLE OF CONTENTS

LIST OF FIGURES

LIST OF TABLES

ACKNOWLEDGMENTS

I would like to thank my parents for their unconditional love and support through the years. They have both worked extremely hard in order to provide me with the life that I have and have always wanted the best for me. They engrained in me from a very young age the importance of compassion and helping others. This lesson has transcended all aspects of my life from wanting to better the biomedical community to my daily habits and interactions with friends and colleagues.

I would like to thank Dr. Bernard Choi for believing in me and for providing me with an opportunity that I consider to be priceless. I started in Bernard's lab as a Biology undergraduate student performing animal surgeries in 2010. I never imagined that I would be in his lab almost a decade later. I believe this is a testament to the lab environment he provides for his students. No one ever wants to leave. His passion for biophotonics is contagious, and he has played a significant role in my desire to attain an advanced degree in Biomedical Engineering. I have learned a lot from him and the experiences that working in his lab has provided, and for this, I am forever grateful.

I would like to thank Dr. Mustafa Kabeer for his patience, support, and advice. I met Mustafa in 2015 as part of a collaboration with our lab and CHOC Children's hospital. From day 1, Mustafa has been the most humble physician I have ever met, especially for someone who has had so much experience and saved so many lives. Mustafa is the embodiment of the ideal physician I would wish to have treating myself, my loved ones, and my future children.

I would like to thank Dr. Gultekin Gulsen for providing me with valuable feedback when I first presented my intended research. His willingness to help and collaborate with my work at CHOC was very much appreciated.

I would like to thank Dr. Tony Durkin and Dr. Gordon Kennedy for their mentorship. I have gone on multiple trips with them to the Institute of Surgical Research in Texas as part of our collaboration. They have taught me a lot about how to properly interact and work with other researcher with diverse backgrounds to achieve a shared goal. Gordon has made these trips more enjoyable with his presence and humor.

I would like to thank Prany Sananikone for his mentorship and guidance. I met Prany in 2010 when he was still working in the Office of Equal Opportunity and Diversity. I have learned many personal and professional lessons over the years from our talks.

I would like to thank my partner, Eileen Lee. She has been very patient, supportive, and understanding as I have gone through grad school. She has made the stressful and exhausting times bearable.

I would like to thank Justin, Wes, and Austin Moy. We have spent many hours in the lab running experiments together, outside of lab on the basketball courts, and they have welcomed me like a younger brother.

I would like to thank the MTI Lab. Dr. Christian Crouzet for being an amazing friend and colleague throughout grad school. Christian's constant willingness to help me with any experiments or troubleshooting has played a big part in the progression of my projects. He is also the most fierce competitor I have come across, and I am very thankful to have won multiple basketball championships playing alongside him. Cody Dunn for his friendship and bringing his enthusiasm, skills, and new ideas to broaden our labs application space. Cody's contribution to my projects have also been substantial with his coding skills. Adrian Bahani for his friendship and work on creating custom 3D printed components for my projects and the continued development of my devices. Dr. Sean White for all of his mentorship and guidance throughout graduate school as well as providing life and career advice. Thank you to all other former and current MTI lab members who have made it a pleasure to come to lab each day and for their help and support on all projects that are discussed in this dissertation as well as the work not mentioned.

I would like to thank all my friends outside of lab who have made my time at UCI an extremely positive experience. I expect these friendships to continue to blossom and grow for many years to come.

I would like to thank the Institute of Clinical and Translational Sciences (ICTS) for their financial support that has allowed me to focus on my research. The resources they have provided me with have also been instrumental in my development as a researcher and professional.

CURRICULUM VITAE

Ben Srun Lertsakdadet

2012 B.S., Biology, University of California, Irvine
2012 B.S., Chemistry, University of California, Irvine
2016 M.S., Biomedical Engineering, University of California, Irvine
2019 Ph.D., Biomedical Engineering, University of California, Irvine

PUBLICATIONS

J.1. Wesley J. Moy, Shreyas J. Patel, **Ben S. Lertsakdadet**, Rajan P. Arora, Katherine M. Nielsen, Kristen M. Kelly, and Bernard Choi, *Preclinical In Vivo Evaluation of NPe6-Mediated Photodynamic Therapy on Normal Vasculature*, Lasers in Surgery and Medicine, 44(2), 158-162, 2012.

J.2. Kristen M. Kelly, Wesley J. Moy, Austin J. Moy, **Ben S. Lertsakdadet**, Justin J. Moy, Elaine Nguyen, Ashley Nguyen, Kathryn E. Osann, and Bernard Choi, *Talaporfin Sodium-Mediated Photodynamic Therapy Alone and in Combination with Pulsed Dye Laser on Cutaneous Vasculature*, Journal of Investigative Dermatology, August 2014, 2-4, 2014.

J.3. **Ben Lertsakdadet**, Bruce Y. Yang, Cody E. Dunn, Adrien Ponticorvo, Christian Crouzet, Nicole Bernal, Anthony J. Durkin, and Bernard Choi, *Correcting for motion artifact in handheld laser speckle images*, Journal of Biomedical Optics, 23(3), 1-7, 2018.

J.4. Cody E. Dunn, **Ben Lertsakdadet**, Christian Crouzet, Adrian Bahani, and Bernard Choi, *Comparison of speckleplethysmographic (SPG) and photoplethysmographic (PPG) imaging by Monte Carlo simulations and in vivo measurements*, Biomedical Optics Express, 9(9), 481-486, 2018.

CONFERENCE PRESENTATIONS AND PROCEEDINGS

C.1. Wesley J. Moy, Shreyas J. Patel, **Ben S. Lertsakdadet**, Rajan P. Arora, Katherine M. Nielsen, Kristen M. Kelly, and Bernard Choi, *Pre-clinical in-vivo evaluation of NPe6-mediated photodynamic therapy on normal vasculature*, in Photonics in Dermatology and Plastic Surgery at SPIE Photonics West, California, January 2012.

C.2. Wesley Moy, **Ben Lertsakdadet**, Rajan Arora, Katherine Nielsen, Kristen Kelly, and Bernard Choi, *Pre-clinical in-vivo evaluation of photodynamic therapy as a potential*

treatment for cutaneous vascular lesions, at American Soceity for Laser Medicine and Surgery, Florida, April 2012.

C.3. Wesley Moy, Justin Moy, **Ben Lertsakdadet**, Kristen Kelly, and Bernard Choi, *Preclinical in-vivo evaluation of combination photodynamic therapy and pulsed dye laser treatment on normal vasculature*, at SPIE Photonics West, California, January 2013.

C.4. Wesley Moy, Justin Moy, **Ben Lertsakdadet**, Kristen Kelly, and Bernard Choi, *Preclinical in-vivo evaluation of combination photodynamic therapy and pulsed dye laser treatment on normal vasculature*, at American Society of Laser Medicine and Surgery, Boston, April 2013.

C.5. Wesley Moy, Justin Moy, **Ben Lertsakdadet**, Kristen Kelly, and Bernard Choi, *Preclinical in-vivo evaluation of combination photodynamic therapy and pulsed dye laser treatment on normal vasculature*, at Montagna Symposium for Biology of the Skin, Washington, October 2013.

C.6. Wesley Moy, Austin Moy, **Ben Lertsakdadet**, Justin Moy, Chelsea Pittman, Gang Ma, Kristen Kelly, and Bernard Choi, *Preclinical in vivo comparison of photodynamic therapy on normal vasculature*, in PanAmerican Photodynamic Association/ASLMS Photodynamic Therapy – Basic Science Section at the American Society for Laser Medicine & Surgery, Arizona, April 2014.

C.7. Wangcun Jia, Joshua Burns, Betty Villantay, **Ben Lertsakdadet**, Bernard J. Choi, Stuart Nelson, and Bahman Anvari, *Encapsulation of Indocynanine Green (ICG) into erythrocyte-derived particles extends the half-life of ICG in mice circulation*, in Nanoparticle Mediated Therapy at American Society for Laser Medicine & Surgery, California, April 2017

C.8. **Ben Lertsakdadet**, Ryan Farraro, Bruce Yang, Christian Crouzet, Adrien Ponticorvo, Anthony J. Durkin, and Bernard Choi. *Handheld Laser Speckle Imaging for Point-of-Care Blood-Flow Measurements*, in Point-of-Care at the American Society for Laser Medicine & Surgery, California, April 2017.

C.9. **Ben Lertsakdadet**, Cody E. Dunn, and Bernard Choi, *Wide-field superficial blood flow imaging using a portable handheld laser speckle imaging device*, in Wound Healing at SPIE Photonics West, California, January 2018.

POSTER PRESENTATIONS

P.1. Wesley Moy, Austin Moy, Justin Moy, **Ben Lertsakdadet,** Kristen Kelly, and Bernard Choi, *Preclinical in-vivo evaluation of combined photodynamic and photothermal therapies*

on normal microvasculature, poster presented at ECI Advances in Optics for Biotechnology, Medicine and Surgery XIII, California, June 2013.

P.2. Wesley Moy, Justin Moy, **Ben Lertsakdadet**, Kristen Kelly, and Bernard Choi, *Preclinical in-vivo evaluation of combination photodynamic therapy and pulsed dye laser treatment on normal vasculature*, poster presented at Montagna Symposium for Biology of the Skin, Washington, October 2013.

P.3. Wesley Moy, Austin Moy Justin Moy, **Ben Lertsakdadet**, Kristen Kelly, and Bernard Choi, *Preclinical in-vivo evaluation of combined photodynamic and photothermal therapies on normal microvasculature*, at UC Irvine Bioengineering Symposium, California, 2014

P.4. **Ben Lertsakdadet**, Bruce Y. Yang, Adrien Ponticorvo, Cody E. Dunn, Christian Crouzet, Rebecca Rowland, Nicole Bernal, Anthony J. Durkin, and Bernard Choi. *In-vitro validation and quantitative measurements of graded burn wounds on a porcine model using handheld laser speckle imaging*, poster presented at ECI Advances in Optics for Biotechnology, Medicine and Surgery XV, Colorado, July 2017.

P.5. **Ben Lertsakdadet**, Bruce Y. Yang, Adrien Ponticorvo, Cody E. Dunn, Christian Crouzet, Rebecca Rowland, Nicole Bernal, Anthony J. Durkin and Bernard Choi. *The progression of a mounted system to a portable, handheld device for wide field blood flow visualization*, poster presented at Institute of Clinical and Translational Science – 2018 Pathways to Cures: Translational Science Research Day, California, May 2018.

P.6. **Ben Lertsakdadet**, Bruce Y. Yang, Cody E. Dunn, Adrien Ponticorvo, Christian Crouzet, Nicole Bernal, Robert J. Christy, Anthony J. Durkin, and Bernard Choi, *Portable, Deployable Blood-Flow Imaging Using Laser Speckle Contrast*, poster presented at Military Health System Research Symposium, Florida, August 2018.

NOTABLE AWARDS AND HONORS

Institute of Clinical and Translational Science – TL1 Pre-Doctoral Scholar (2016)

ABSTRACT OF THE DISSERTATION

Accounting for Motion Artifact and Optical Property Changes
in Laser Speckle Imaging

By

Ben Srun Lertsakdadet

Doctor of Philosophy in Biomedical Engineering

University of California, Irvine, 2019

Professor Bernard Choi, Chair

Quantitative characterization of blood flow is important to assess acute physiological health and hemodynamic effects of clinical interventions. A critical need exists for a robust device designed to assess blood flow in biomedical applications. Laser Speckle Imaging (LSI) is a wide-field non-invasive optical technique that enables superficial blood flow quantification. A few potential clinical applications of LSI include assessing blood flow during burn patient triaging, quantifying tissue perfusion in a neonatal intensive care unit, and real-time blood flow mapping during surgery. The blood flow information that LSI provides can be helpful for bedside care. However, since LSI systems are highly sensitive to motion, most LSI studies are typically performed using mounted systems. Widespread use of LSI in the clinic has not occurred, in part, due to the bulky form factor and lack of mobility of these systems.

Our proposed solution to address the limitations of these mounted systems is a handheld LSI device. Handheld LSI would provide clinicians with objective blood flow measurements in a convenient form factor. However, motion artifact during handheld data acquisition can lead to unreliable and inaccurate blood flow values. Attempts have been

made to account for motion artifact noise, but they lack an approach to align (co-register) images. Co-registration is a necessary step prior to the common practice of image averaging to improve the signal-to-noise ratio in producing blood flow maps. Our approach to address both motion artifact and image co-registration for handheld LSI was adding a fiducial marker (FM) into our imaging protocol.

We developed a portable, handheld LSI device and a protocol that integrated a FM into the imaging workflow. We automated the processes of sorting frames based on motion artifact and co-registering misaligned images. We compared the performance of the mounted and handheld setups using *in vitro* flow phantom experiments as a proof-of-concept study. We then demonstrated translation of our imaging protocol into an ongoing *in vivo* study with a porcine burn wound model.

We attempted to further reduce motion artifact by making additional modifications to the handheld LSI device. The modified LSI device was also validated with *in vitro* flow phantom experiments and *in vivo* imaging of vessels within a dorsal skinfold window chamber model.

In addition to the concerns of motion artifacts for clinical imaging, optical property changes in dynamic wounds or developing tissues may cause inaccuracies in the measured blood flow. We addressed this issue by combining LSI and Spatial Frequency Domain Imaging (SFDI), a non-contact imaging modality used to quantify tissue optical properties, to obtain corrected blood flow values. We then showed the potential errors in blood flow values when optical properties are not properly accounted for in the dynamic wounds of a porcine burn wound model.

Collectively, these works demonstrate our attempts at providing a viable alternative for clinical blood flow imaging with our handheld LSI device and imaging protocol and accounting for motion artifact and optical property changes in LSI.

INTRODUCTION

Normal functional intestine is necessary to provide nutrients, electrolytes, and fluid requirements. In neonates, receiving an adequate amount of these supplies is even more important in order to not only sustain, but also propagate growth and development. Insufficiencies in absorbing and transporting these compounds can lead to malnutrition, which can cause neurodevelopmental complications and other developmental issues. This state of inability to absorb enough nutrients to sustain and propagate growth is known as intestinal failure (IF)[1].

In the case of intestinal failure (IF), there is a reduction in functional intestinal mass, which leads to a lack of intestinal nutrition[1].In a study of 272 preterm infants followed for a period of 27 months, 73 patients died (27% mortality rate), which demonstrates the severity of IF[2]. The cause of death in majority of the cases (n=58) was multiorgan system failure; emphasizing the importance of the intestine to absorb and transport nutrients to the rest of the body for metabolic processes[2]. IF leads to malnutrition which is the cause for other neurodevelopmental, wound healing, and health complications. Other intestinal conditions include gastrointestinal infection, gastroschisis, atresia, aganglionosis, volvulus, and necrotizing enterocolitis (NEC), all of which are associated to abnormal blood flow to the intestine and can lead to IF[1,2]. Since adequate blood flow to all living tissue within the body is essential for oxygen transport and sustaining metabolic demands[3], developmental issues or injuries that lead to inadequate adequate blood supply, or ischemia, can lead to infection and necrosis[3]. Therefore, proper quantification of blood flow is important for assessing physiological health and hemodynamics associated with clinical symptoms.

Current methods of assessment used at Children's Hospital of Orange County (CHOC) include the physician checking the abdomen for redness, tautness, and inflammation in appearance. These are all potential signs of infection of the intestine. Physical examination of the abdomen may also reveal tenderness in the subcutaneous layer, edema, induration, or peritonitis, which further indicate that the issue lies deeper. Unfortunately, the only way to positively identify that a specific part of the intestine is ischemic is during surgery when the bowels are fully exposed. Even at this point in assessment, distinguishing healthy from ischemic tissue is purely subjective.

There is currently no objective way to thoroughly assess the progression of IF in neonates, and clinicians are forced to rely upon physical observations. This is partially due to neonates being a vastly understudied patient population; therefore, there is a shortage in neonate specific treatment for many health conditions[4]. With the lack of an objective method for diagnosing IF, physicians are at a disadvantage for treating this complex condition. Thus, a critical need exists for a robust device designed to quantify blood flow in a wide range of biomedical applications. We propose Laser Speckle Imaging (LSI) as the imaging modality to fulfill this need.

LSI is a wide-field non-invasive optical technique that enables superficial blood flow quantification[5–7]. It requires a camera (CCD) with a lens for imaging, a diffuse laser source, and a computer for processing the data (Fig. 0.1). In LSI, a speckle contrast value, K, is computed through the following relationship:

$$K = {}^{\sigma}/_{\langle I \rangle} \qquad \text{(Eq. 0.1)}$$

where σ is the standard deviation of the intensity values of the pixels within a sliding window, and <I> is the mean intensity of the same window.

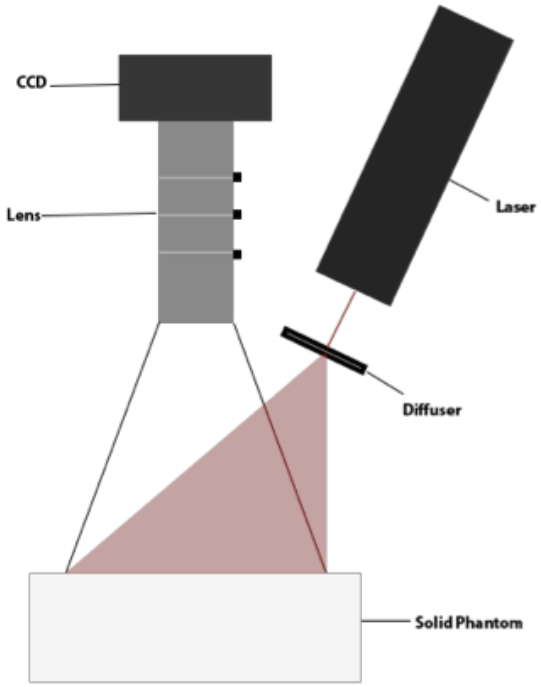

Figure 0.1: Example of Laser Speckle Imaging (LSI) set-up.

In a static sample, the speckle pattern is preserved and results in bright and dark spots as a result of constructive and destructive interference of coherent light as it interacts with the sample (Fig. 0.2a). When motion/movement occurs, a blurring of the speckle pattern is observed (Fig. 0.2b).

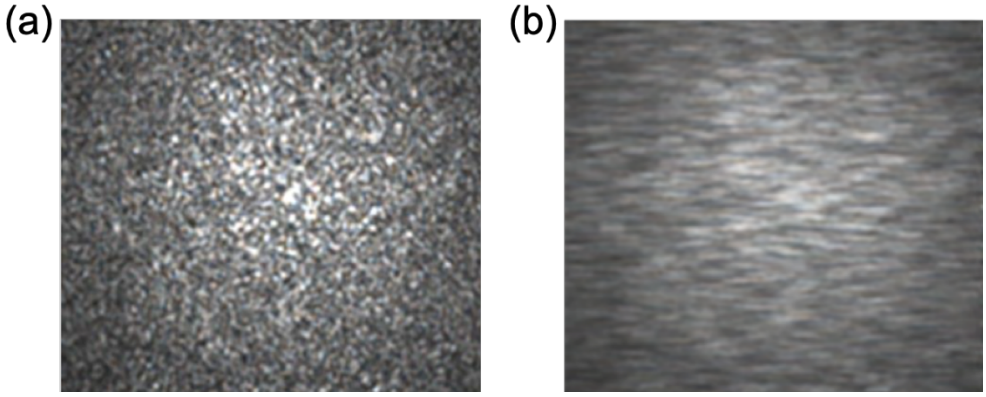

Figure 0.2: Speckle pattern of a stationary vs moving tissue phantom. (a) A raw image of a tissue phantom showing the preservation of the speckle pattern when the phantom remains stationary. (b) The speckle pattern is blurred when the phantom is moved.

LSI was first discussed in a publication by Fercher and Briers who used it for flow visualization in single exposure photography[8]. Boas and Dunn[6] discussed the theoretical background behind LSI that was previously published by Briers and Webster[5] where K is a function of exposure time, T, and is related to the autocovariance of the intensity fluctuation in a single speckle, $C_t(\tau)$, by:[6]

$$K^2 = \frac{\sigma_s^2(T)}{\langle I \rangle^2} = \frac{2}{T\langle I \rangle^2} \int_0^T \left(1 - \frac{\tau}{T}\right) C_t(\tau) d\tau \qquad \text{(Eq. 0.2)}$$

If speckle correlation time is defined as:[9]

$$\tau_c = \int_{-\infty}^{\infty} |\gamma(t)|^2 dt \qquad \text{(Eq. 0.3)}$$

where $\gamma(t)$ the normalized autocorrelation function of the reflected laser light. Assuming a Gaussian velocity distribution for ordered flow, K becomes:

$$K = \left[\frac{1}{2}\frac{\tau_c}{T} \operatorname{erf}\left(\pi^{1/2} \frac{T}{\tau_c}\right)\right]^{1/2} \qquad \text{(Eq. 0.4)}$$

to achieve maximum sensitivity of K, T is chosen to be comparable to τ_c. We then use the following relationship to equate K to speckle flow index (SFI):

$$SFI = \frac{1}{2K^2 T} \qquad \text{(Eq. 0.5)}$$

which has been shown to correlate linearly with flow speeds ranging from 2 to 20mm/s when T is 1ms and 0 to 5mm/s when T is 10ms[10]. Figure 0.3 shows the processing method from a set of RAW images to the Speckle Contrast map, and finally, to the Speckle Flow Index map, which is proportional to $1/K^2$.

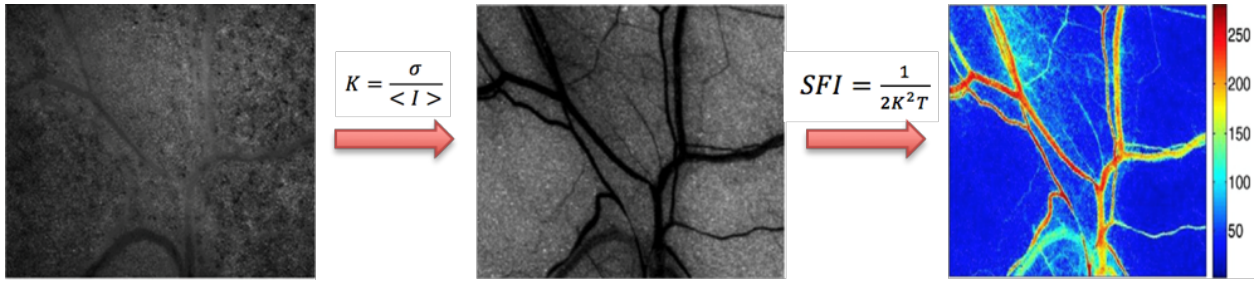

Figure 0.3: Processing method of converting a raw image to a speckle contrast (K) image to a speckle flow index (SFI) image.

In a research setting, some applications of LSI include measuring blood flow in the animal brain during externally stimulated conditions [11], measuring blood flow in a window chamber as a response to therapies [12–14], and measuring blood flow in varying severities of induced burn wounds [15,16]. In a clinical setting, LSI can also provide assistance in assessing medical conditions such as peripheral vascular disease [17], diabetes [18], and burn wounds at the bedside through measured blood flow [19]. In addition, LSI is capable of providing real-time blood flow mapping during surgery[20–23]. However, since LSI systems are highly sensitive to motion, most LSI studies are typically performed using mounted systems. Widespread use of LSI in the clinic has not occurred, in part, due to the bulky form factor and lack of mobility of these systems.

Can we create an alternative form factor of a LSI device that will address the current limitations of mounted systems? How do we account for motion artifact (Chapter 1)?

Our proposed solution to address the limitations of these mounted systems is a handheld LSI device. Handheld LSI would provide clinicians with objective blood flow

measurements in a convenient form factor. However, motion artifact during handheld data acquisition can lead to unreliable and inaccurate blood flow values. Attempts have been made to account for motion artifact noise, but they lack an approach to align (co-register) images. Co-registration is a necessary step prior to the common practice of image averaging to improve the signal-to-noise ratio in producing blood flow maps. Our approach to address both motion artifact and image co-registration for handheld LSI was adding a fiducial marker (FM) into our imaging protocol.

We previously developed a portable, handheld LSI device, but the field of view (FOV) was only 25mm x 18.7mm, the system used a 650nm laser pointer, and motion artifact was not quantifiable[24]. We made significant changes to the handheld LSI device which included machining custom components to allow the handheld LSI device to be easily mounted to a tripod, switching to a near infrared laser (809nm) and adding a long pass filter for data acquisition with room lights turned on, and increasing the FOV to 90mm x 67.5mm. We changed our imaging workflow by placing a FM into the FOV of our handheld LSI device. The FM played two roles in addressing motion artifact.

First, by determining the K value of the FM, K_{FM}, with a mounted system, we can determine the amount of motion artifact by quantifying the reduction of K_{FM} in each frame. This allowed us to sort the images within each data set and identify useable frames by determining a cut-off or threshold value for K_{FM}. Second, we were able to use the FM within each image to co-register useable frames even if they were translationally shifted. We automated the processes of sorting frames based on motion artifact and co-registering misaligned images.

We compared the performance of the mounted and handheld setups using *in vitro* flow phantom experiments as a proof-of-concept study. The results from these experiments showed that handheld LSI, once we accounted for motion artifact, is comparable to mounted LSI. We then demonstrated translation of our imaging protocol into an ongoing *in vivo* study with a porcine burn wound model. We imaged superficial and full thickness burn wounds and quantified the blood flow within the burn region. Without using the FM to account for motion artifact, handheld LSI device was not able to distinguish the difference between a superficial and full thickness burn wound. However, when the FM was utilized, handheld LSI data was comparable to mounted LSI data and we were able to distinguish the difference between superficial and full thickness burns. Although the results of this study showed the viability of the a handheld LSI device, we wanted to further reduce motion artifact.

If we incorporate a handheld gimbal stabilizer (HGS), can we further reduce motion artifact utilizing our handheld LSI device paired with our FM imaging protocol (Chapter 2)?

We attempted to further reduce motion artifact by incorporating a HGS to the handheld LSI device. HGS are commonly used in photography and videography to reduce shakiness and vibrations associated with handholding a camera. Adding a HGS to a LSI device, which we called the Motion Stabilized LSI (msLSI) device, is a novel concept that we wanted to test. Recently, another group published on the "stabilized" use of handheld LSI device to quantify retinal blood flow, but their stabilized condition was actually referring to a mounted condition in which the device was attached to a table[25].

In addition to the HGS, we increased the FOV to 140mm x 105mm, which would be desirable for measuring larger samples in a clinical setting. We compared the handheld use

of our msLSI device with and without the HGS using *in vitro* flow phantom experiments. The msLSI device showed improved K compared to handheld LSI without the HGS at all flow speeds. The mean number of images above the threshold K_{FM} value was also significantly greater when using the msLSI device.

To test a more extreme case, we reduced the FOV of the msLSI device to 20mm x 15mm to image the vasculature in a dorsal skinfold window chamber model. For these *in vivo* experiments, we also developed an image processing workflow that automated the identification of the window chamber, sorted images based on the mean K of the tissue within the window chamber (K_{WC}) , and aligned all images using the window chamber. In doing so, the tissue within the window chamber acted as the FM for these experiments. Using the msLSI device resulted in a greater number of images above a threshold K_{WC} value compared to handheld LSI without the HGS. We wanted to compare the signal-to-background ratio (SBR) of the average SFI images that resulted from the msLSI and handheld without HGS data sets. The signal was determined from the SFI value from the vessels and the background was determined from the SFI value from the background tissue. Less motion artifact is associated with higher SBR, and msLSI data resulted in higher SBR compared to handheld without HGS. We were able to show that by pairing a HGS with handheld LSI, we could further reduce motion artifact in handheld LSI data acquisition.

In addition to motion artifact concerns for LSI imaging, optical property changes in dynamic wounds can also lead to inaccuracies in measured blood flow. This is an issue for currently commercialized, mounted LSI devices as well.

How will optical property changes in dynamic wounds affect the measured blood flow by an LSI device (Chapter 3)?

LSI has been utilized for measuring blood flow in burn wounds for assessing burn severity. However, burn wounds are highly dynamic wounds making them an ideal model for comparing the effects of optical property changes on actual blood flow. The American Burn Association approximates 450,000 burn injuries occur in the United States annually[26]. Current clinical protocol for assessing these burn wounds are based on visual observations by an experienced surgeon, which can be subjective[27–29]. The dynamic nature of burn wounds within the first 48-72 hours makes them extremely difficult to diagnose accurately[30]. However, early and accurate assessment of burn wounds is vital for determining the path of treatment and outcome of the wound[31–33].

Although studies have shown that blood perfusion is an adequate method for assessing burn wounds, they do not take into account the structural changes that occur. A non-contact imaging modality capable of quantifying these structural changes is Spatial Frequency Domain Imaging (SFDI). SFDI is an imaging technique that provides optical properties of tissue (reduced scattering coefficient, μ_s', and absorption coefficient , μ_a) along with oxy- and deoxy-hemoglobin information[34–39]. SFDI utilizes a spatial light modulator, such as a digital micromirror (DMD) or liquid crystal on silicone (LCOS) device, to project light with spatially varying patterns[35]. The reflected light captured by the CCD camera can be interrogated to determine the optical properties by processing individual pixels using a photon propagation model[35]. The spatially projected light takes on the form:[35,40]

$$I_{IN} = \frac{S_0}{2}[1 + M_0 cos(2\pi f_x x + \propto)] \qquad \text{(Eq. 0.6)}$$

where S_0 is the illumination source intensity, M_0 is the modulation depth, f_x is the spatial frequency, and α is the spatial phase. The reflected light takes on the form:[35,40]

$$I_{OUT} = M_{AC}(x)\cos(2\pi f_x x + \propto) + I_{DC} \quad \text{(Eq. 0.7)}$$

where $M_{AC}(x)$ is the envelope function that modifies the reflected photon density wave. The $M_{AC}(x)$ is a product of the source intensity and the modulation transfer function (MTF) of the sample (R_d) and imaging system (MTF_{system}):[35]

$$M_{AC}(x_i) = I_0 \cdot MTF_{system}(x_i) \cdot R_d(x_i) \quad \text{(Eq. 0.8)}$$

A reference/calibration measurement is taken using a tissue phantom with known optical properties and allows us to recover the diffuse reflectance. A Monte Carlo light-transport model is then used in conjunction with a lookup table to determine optical properties at each pixel[35,40].

We hypothesized that by utilizing SFDI to determine optical property of the burn wounds, we can improve the accuracy of the perfusion information measured by LSI. We attempted to quantify the error in LSI measured perfusion units when (1) the dynamic optical properties are determined and used to correct perfusion units (2) the pre-burn optical properties are used to correct perfusion units and (3) commonly assumed optical properties are used to correct perfusion units. In addition, we attempted to use LSI to correlate perfusion measurements immediately post-debridement with successful vs failed outcome of varying burn severity and debridement depths.

We showed that the errors associated with assuming optical properties or using the optical properties from a single time point can lead to a high error in measured blood flow to the actual characterized diffusion (D_B) value associated with the imaged tissue.

Collectively, these works demonstrate our attempts at providing a viable alternative for clinical blood flow imaging with our handheld LSI device and imaging protocol and the importance of properly accounting for motion artifact and optical property changes in LSI. With these considerations, a msLSI device may be suitable for clinical use to assist physicians in assessing patients in the neonatal intensive care unit (NICU) and burn unit.

CHAPTER 1: Correcting for motion artifact in handheld laser speckle images

This work was originally published in Journal of Biomedical Optics.

1.1 Abstract

Laser Speckle Imaging (LSI) is a wide-field optical technique that enables superficial blood flow quantification. LSI is normally performed in a mounted configuration to decrease the likelihood of motion artifact. However, mounted LSI systems are cumbersome and difficult to transport quickly in a clinical setting for which portability is essential in providing bedside patient care. To address this issue, we created a handheld LSI device using scientific grade components. To account for motion artifact of the LSI device used in a handheld setup, we incorporated a fiducial marker (FM) into our imaging protocol and determined the difference between highest and lowest speckle contrast value for the FM within each data set (K_{best} and K_{worst}). The difference between K_{best} and K_{worst} in mounted and handheld setup was 8% and 52%, respectively, thereby reinforcing the need for motion artifact quantification. When using a threshold FM speckle contrast value (K_{FM}) to identify a subset of images with an acceptable level of motion artifact, mounted and handheld LSI measurements of speckle contrast of a flow region (K_{FLOW}) in an *in vitro* flow phantom experiments differed by 8%. Without use of the FM, mounted and handheld K_{FLOW} values differed by 20%. To further validate our handheld LSI device, we compared mounted and handheld data from an *in vivo* porcine burn model of superficial and full thickness burns. The speckle contrast within the burn region (K_{BURN}) of the mounted and handheld LSI data differed by <4% when accounting for motion artifact using the FM, which is less than the speckle contrast difference between superficial and full thickness

burns. Collectively, our results suggest the potential of handheld LSI with a FM as a suitable alternative to mounted LSI, especially in challenging clinical settings with space limitations such as the intensive care unit.

1.2 Introduction

Laser Speckle Imaging (LSI) is a wide-field optical technique that enables superficial blood flow quantification. Pre-clinical applications of LSI include blood flow monitoring in rodent skin[12–14,41] and in porcine burn models[15]. Potential clinical applications include blood flow monitoring in patients undergoing treatment of port-wine stains[21] and breast tissue perfusion during radiation therapy[42]. A coherent light source (laser) is used to illuminate a tissue region of interest. LSI devices typically use a two-dimensional sensor array (camera) to capture the interference pattern detected at the imaging sensor plane. The resulting fluctuations in the pattern can be quantified to provide maps of relative blood flow.

Blood-flow information can be helpful in a clinical setting for bedside care. However, since the speckle pattern is sensitive to motion, LSI systems are conventionally designed as mounted, or immobile, often mounted on a tripod or a cart with articulating arm (PeriCam PSI System, Perimed AB, Järfälla, Sweden). Hence, widespread use of LSI in the clinic has not occurred due to the bulky form factor and lack of mobility of the system.

Our proposed solution to address the limitations of these mounted systems is a handheld LSI device. Handheld LSI would provide clinicians with objective blood flow measurements in a convenient form factor. However, using an LSI device in a handheld setup introduces problems due to motion artifact from the user end, which leads to unreliable and inaccurate data observed as variable speckle contrast (K) values. Attempts

have been made to account for motion artifact noise. Farraro *et al*[24] found that if a particular number of images is acquired per data set, the coefficient of variation in speckle contrast can be reduced below 5%. Omarjee *et al*[43] used adhesive opaque surfaces (AOS) for signal identification during post processing of collected LSI data. The AOS was used to denoise LSI data collected to measure cutaneous blood flow.

Although these methods attempt to account for motion artifact, they both lack incorporation of an approach to align (co-register) images. Co-registration is a necessary step prior to the common practice of image averaging to improve the signal-to-noise ratio in LSI flow maps. Our approach to address both motion artifact and image realignment for handheld LSI is incorporation of a fiducial marker (FM) into our imaging protocol. We hypothesize that by using a FM, we are able to collect LSI data using a handheld device that approximates the performance of a mounted/fixed LSI system.

The FM should fulfill the following criteria: 1) it must have a reproducible measured speckle contrast value that can be accurately characterized in a mounted setup; 2) as in Omarjee *et al*[43], the FM must have sufficient thickness and optical scattering to ensure that the K of the FM (K_{FM}) is independent of the underlying tissue; and 3) it must have sufficiently different optical properties from the surrounding tissue regions to facilitate unambiguous identification of the FM during image realignment.

Here we demonstrate that with integration of a FM into the imaging protocol executed with a handheld LSI device, we can improve the accuracy of K values towards those measured with a gold-standard mounted setup. We compare the performance of the mounted and handheld setups using *in vitro* flow phantom experiments as a proof-of-

concept study. We then demonstrated translation of our imaging protocol into an ongoing *in vivo* study with a porcine burn wound model.

1.3 Materials and Methods

1.3.1 Handheld Laser Speckle Imaging Device

The handheld laser speckle imaging (LSI) device (Fig. 1.1) used in all of the experiments consisted of an 8-bit, 1.32 megapixel CCD camera (CMLN-13S2M-CS, FLIR Integrated Imaging Solutions, Inc., Richmond, BC, Canada) acquiring 640 x 480 pixel frames at 15Hz as the imaging sensor. An imaging field of view (FOV) of approximately 90mm x 67.5mm (4:3 ratio) at an imaging distance of 300mm was obtained using a C-mount lens (Computar C-Mount 13-130mm Varifocal Lens, Computar). Imaging parameters were selected to achieve ~3 pixels per speckle, thus satisfying the Nyquist sampling criterion[10]. The data were collected and processed on a tablet computer (Microsoft Surface Pro 2, Microsoft Inc.) using a custom-written GUI in MATLAB (The Mathworks, Natick MA).

The coherent light source was an 809nm near-infrared laser diode (140mW, Ondax Inc., Monrovia, CA) positioned at a slightly oblique angle to assist with alignment. A 300mm ruler was used to check the distance from the LSI device and the sample being measured. If the device were too close during data acquisition, the irradiated region would shift towards the upper left quadrant in the FOV; if the device were too far, the irradiated region would shift towards the lower left quadrant. Data acquisition was initiated only after the irradiation region was in the approximate center of the FOV. The exposure time used for each image was 5ms, based on the findings of Farraro *et al*.[8]

The tablet was placed inside a protective case (Urban Armor Gear), which was modified to allow direct mounting of the lens, camera, and laser to the tablet. The device was designed for use in both mounted and handheld configuration.

1.3.2 Fiducial Marker

The fiducial marker (FM) was a 18% reflectance grey card (Neewer, model #10079934) commonly used in photography. The FM was used to sort and align the acquired images (see Section 1.3.3). It was attached to the surface of a solid silicone phantom (see Section 1.3.4) and imaged using our LSI device in mounted and handheld setups (Fig. 1.1a,b). Each data set contained 150 images for analysis. All images were converted into spatial speckle contrast (K) images using a 7 x 7 pixel sliding window with the equation $K=\sigma/\langle I\rangle$, where K is the contrast, σ the standard deviation within the window, and $\langle I\rangle$ the mean intensity of the pixels contained within the window[12,13,21,41]. K_{FM} was quantified from each image.

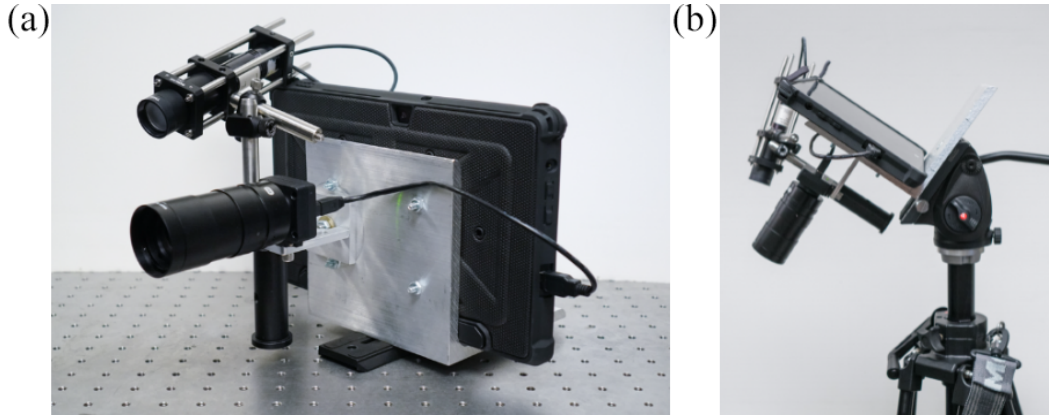

Figure 1.1: Assembled handheld LSI device. (a) Fully assembled device and (b) device in a tripod-mounted setup.

1.3.3 Estimation of Motion Artifact and Image Alignment using FM

Motion artifact was estimated using the quantified K_{FM} in each image. All images within a data set were sorted in descending order based upon the K_{FM} associated with each image.

This approach was based on the assumption that with increasing motion artifact, K_{FM} would decrease from the "true" value (0.50, in this study) measured with the mounted LSI setup. We set arbitrary threshold K_{FM} differences of 10% and 20% (i.e., $K_{FM,thres}$=0.45 and 0.40, respectively) and determined the number of images in the collected data sets whose K_{FM} values exceeded the threshold, and the corresponding K values of a specified region of interest (ROI) extracted from the subset of images (see Sections 1.3.4 and 1.3.5 below). As a comparison, average K images were also created using all 150 images to compare differences in average K_{FM} values using the FM-based approach and an unsupervised approach.

Prior to ROI extraction from a given subset of LSI images, we used the FM to align the LSI images using custom-written MATLAB software. First, a median sliding filter with a 7 x 7 pixel window filter was run on each of the images. Next, the software calculated the necessary transformation matrices. The transformation matrices were found by performing a translation, rotation, and scaling in multiple axes to align each raw image to the highest ranked raw image.[11] These transformation matrices were created by combining MATLAB functions with our custom-written software. We converted the raw images to spatial K images and then used the transformation matrices on their respective K images.

1.3.4 *In vitro* Flow Phantom

Flow phantom experiments were performed using a solid silicone phantom created with the methods outlined in Ayers *et al*.[12] We also incorporated a clear plastic tube (diameter 10mm) as a surface-level inclusion flow tube. The flow medium was a 1% Intralipid solution (Fresenius Kabi) infused into the flow tube using a mechanical pump (NE-1000 Single Syringe Pump, Pump Systems Inc.). Two ranges of flow speeds were used:

1) 0.0 to 1.0mm/s, in 0.2mm/s increments; and 2) 1 to 5mm/s in 1mm/s increments. Sequences of 150 images were acquired using mounted and handheld setups at each flow speed. As described in the previous section, K_{FM} was identified based on specified threshold values and aligned using the FM, followed by quantification of K within a ROI selected inside the flow tube (K_{FLOW}). The difference in K_{FLOW} resulting from data collected with mounted and handheld setups was determined. Bland-Altman analysis[13] was performed with Prism 7 software (GraphPad Software, Inc.) to study the measurement performance of the handheld and mounted LSI setups.

1.3.5 *In vivo* Mounted Versus Handheld Imaging of Porcine Burn Wound Model

All experiments were performed in accordance with the Animal Care Use Committee of University of California, Irvine (IACUC # 2015-3154). We performed a graded burn wound experiment using a porcine model described previously.[5] Briefly, 30mm diameter burns were created using a brass tool heated to 100°C. The burn severity was based upon the contact time of the burn tool to the porcine skin. Contact time was varied from five seconds (superficial) to 40 seconds (full thickness) to generate a full range of burn severities (16 burns per pig, two pigs). For *in vivo* validation of the handheld LSI approach, we collected data from both superficial and full thickness burns. Each data set was acquired with mounted and handheld LSI setups and contained 100 images to reduce acquisition time. The FM was placed in the FOV of the images and K_{FM} calculated from each image. An average K image was created using the sort, threshold, and align methods described above. Quantification of K from a ROI within each burn (K_{BURN}) was performed and compared for mounted and handheld setups.

1.4 Results

1.4.1 KFM is indicative of motion artifact

To investigate the influence of motion artifact on handheld LSI measurements, the FM was included in all images acquired for each data set (Fig. 1.2a). The K_{FM} on a static phantom was quantified with mounted and handheld setups. The true K_{FM} measured with the mounted LSI setup was 0.50. After imaging the marker with these solid phantoms, we sorted the K values of the FM in descending order. K_{FM} decreased more quickly in handheld measurements than in mounted measurements (Fig. 1.2b). The relative stability of the K_{FM} across the mounted data set (Fig. 1.2b), compared to a handheld data set (Fig. 1.2b), demonstrated the sensitivity of K values to motion artifact. Please note that the reduction in K_{FM} in the mounted data set was associated with the button press on the tablet screen to initiate data acquisition. The image with the highest K_{FM} value was considered the "best" image and contained the least motion artifact (K_{best}). The image with the lowest K_{FM} value was considered the "worst" image and contained the most motion artifact (K_{worst}). To analyze the range of motion artifact within each data set, the percent difference between K_{best} and K_{worst} was calculated. In the mounted setup, the percent difference was found to be 8%, whereas the percent difference in the handheld setup was 52%. Furthermore, K_{best} measured with the handheld setup (0.47) was lower than the true K_{FM} value, demonstrating that, even in the best-case comparison, user motion introduces an error.

We then applied threshold K_{FM} ($K_{FM,thres}$) values to identify subsets of images with K_{FM} differences ranging between 0 and 20% (Fig. 1.2c). As expected, the number of images in each subset decreased as $K_{FM,thres}$ approached the true K_{FM} value. The maximum K_{FM} value from the handheld data sets consistently was below the true K_{FM} value,

demonstrating that some motion artifact was present within each image of the handheld data sets. Collectively, these data demonstrate the issues related to motion artifact. If we were to use all of the images within a handheld data set to quantify the mean K of a ROI, the handheld setup would potentially result in grossly inaccurate K values.

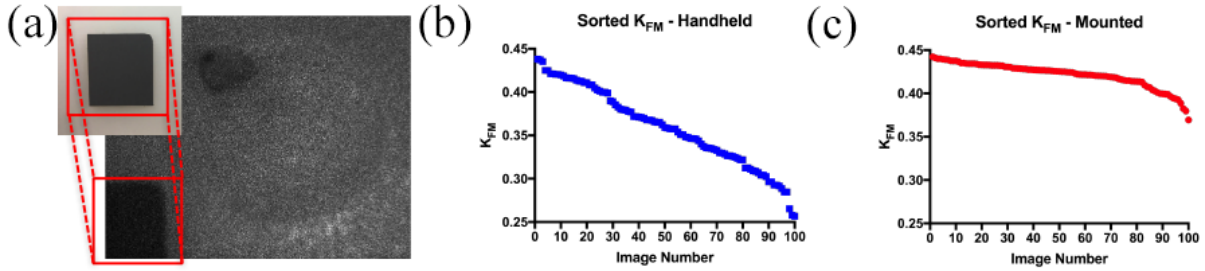

Figure 1.2: Fiducial marker included into imaging protocol allows for motion artifact detection based on speckle contrast (K). Fiducial marker included into imaging protocol allows for motion artifact detection based on speckle contrast (K). (a) The 18% gray card used in our imaging protocol was placed in the lower left hand corner of all frames during data acquisition to allow for sorting based upon motion artifact and image alignment when calculating average speckle contrast images. Here, the FM was placed on the surface of a flow phantom. The FM was identified and the speckle contrast value of the FM (KFM) was quantified and plotted in descending order for all images within each data set. (b) The handheld KFM values plotted show a rapid decline within a representative sorted handheld data set. The KFM mounted values plotted remain relatively stable across all images within a sorted mounted data set. (c) The table shows the number of images in the handheld data set that satisfies each selected KFM values and how these KFM values are related to the mounted KFM in terms of percent difference.

1.4.2 Using the FM to account for motion artifact improves accuracy of K values calculated from data acquired with the handheld LSI setup

To investigate how the FM can help with motion artifact correction, the image processing protocol outlined in section 1.3.3 was applied to use the FM to identify images with the least motion artifact. We first compared the mounted LSI data with K_{FM} = 0.50 (i.e., data with no motion artifact) with handheld LSI data using all images, to mimic unsupervised analysis of the data; the median difference in K values from a ROI centered on the flow tube inclusion (K_{FLOW}) was 20% (range: 7-26%) (Fig. 1.3a). We then applied $K_{FM,thres}$ values of 0.45 and 0.40 to extract subsets of images with K_{FM} values above these thresholds, to analyze further. Each image subset was then aligned using the FM. Using

$K_{FM,thres}$ of 0.45 and 0.40 resulted in median differences in K_{FLOW} values of 5% (range:1-12%) and 8% (range: 0.3-16%), respectively (Fig. 1.3b), demonstrating the improved accuracy resulting from use of the FM. Bland-Altman analysis with the two thresholds showed biases in K_{FLOW} values of -0.0051 and -0.014 for $K_{FM,thres}$ of 0.45 and 0.40, respectively (Fig. 1.3(c-d)). Since the 95% confidence limits of agreement with both $K_{FM,thres}$ values are similar (-0.023 to 0.0047 for $K_{FM,thres}$ = 0.40; -0.031 to 0.0029 for $K_{FM,thres}$ = 0.45), we selected $K_{FM,thres}$ = 0.40 to apply in the subsequent *in vivo* study described in the next section.

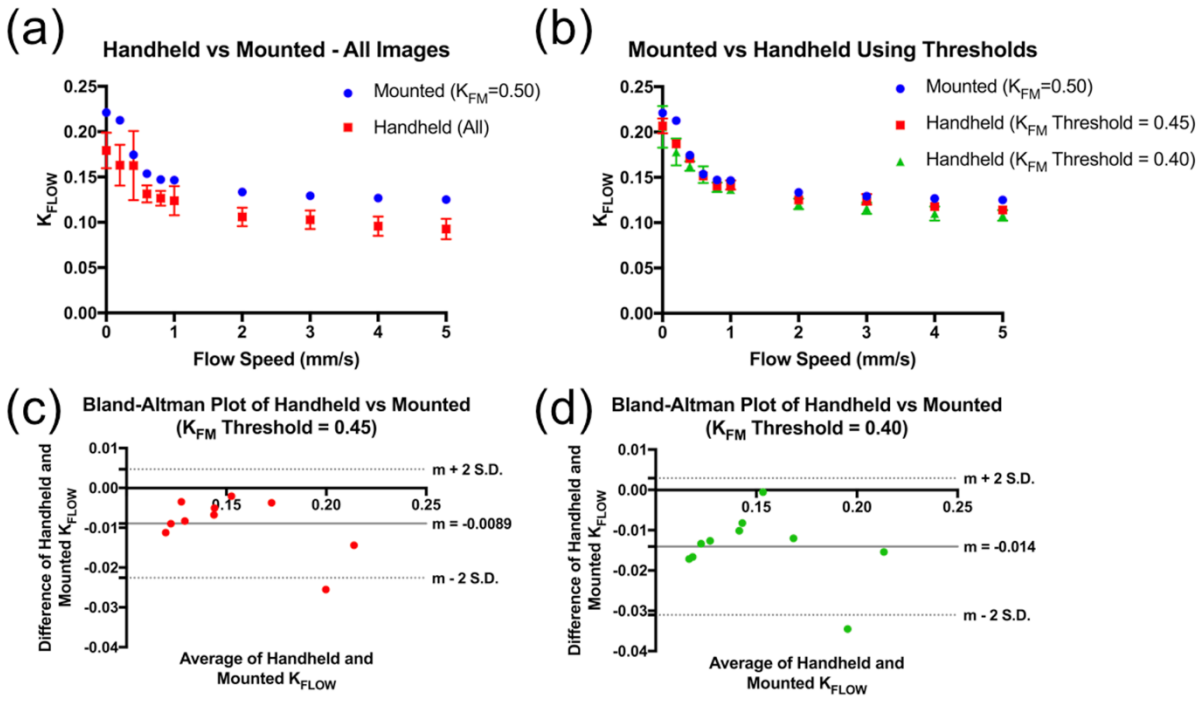

Figure 1.3: K values of handheld and mounted setups from in vitro flow phantom experiments. (a) With an unsupervised approach, use of all 150 handheld LSI images resulted in an error of up to 20%. (b) When using the FM to select a subset of images with a minimum K_{FM} value to account for motion artifact and to re-align images, the accuracy of handheld LSI improves, with errors of 8 and 5% for K_{FM} values of 0.40 and 0.45, respectively. (c) Bland-Altman plot of K_{FM} data collected using $K_{FM,thres}$ = 0.40. We observed a systematic bias of -0.0051 between the two measurement approaches (95% confidence limits of agreement = -0.023 to 0.0047. (d) Bland-Altman plot of K_{FM} data collected using $K_{FM,thres}$ = 0.45. We observed a systematic bias of -0.014 between the two measurement approaches (95% confidence limits of agreement = -0.031 to 0.0029).

1.4.3 Accounting for motion artifact with the FM improved handheld LSI performance: *in vivo* porcine burn model

To determine the translational potential of the *in vitro* findings to *in vivo* use, we imaged porcine burn wounds. Fig. 1.4(a-b) shows a comparison of speckle contrast maps calculated from speckle image sequences captured with the mounted LSI setup, either without (Fig. 1.4a) or with (Fig. 1.4b) use of the FM to align the images. Without alignment, the speckle contrast map appears blurred due to movement occurring during data collection. In this specific case, the K values were only slightly affected without use of the FM [median difference in K values of 2% (range:0.1-4.0%)], which may have been due to the homogeneity of K values within the burned region. In a more heterogenous flow map, the accuracy is expected to degrade without use of an alignment technique.

We used our FM and processed the handheld data using $K_{FM,thres}$ of 0.40. This resulted in 10.2 ± 5.4 images used to create the speckle contrast map. Due to motion artifact resulting from subject breathing, K_{best} collected with the mounted setup was 0.46, which is less than the true FM value of 0.50. Hence, we also applied $K_{FM,thres}$ of 0.40 to the mounted LSI data sets.

By imaging superficial and full thickness burns using the LSI device in mounted and handheld setups, we determined the magnitude of K values measured within the burn (K_{BURN}) for both imaging setups. On day 1 post-burn, the percent difference of K_{BURN} between the mounted and handheld data was 4% for each burn type. In contrast, K_{BURN} of full-thickness burns was 27% higher than that of superficial burns (Fig. 1.4c).

On the final day (day 4) of imaging, the burn wounds have stabilized and are more indicative of the burn type[15]. The percent difference of K_{BURN} on day 4 for mounted versus

handheld was ~1%. K_{BURN} of full-thickness burns was 32% higher than that of superficial burns. These data suggest that, regardless of mounted or handheld LSI setup, we still were able to use K values alone to differentiate between a superficial and full thickness burn. Without use of the FM to threshold and align the LSI images, handheld LSI reported K_{BURN} values that were ~20% lower (range:16-25%) than handheld LSI with use of the FM.

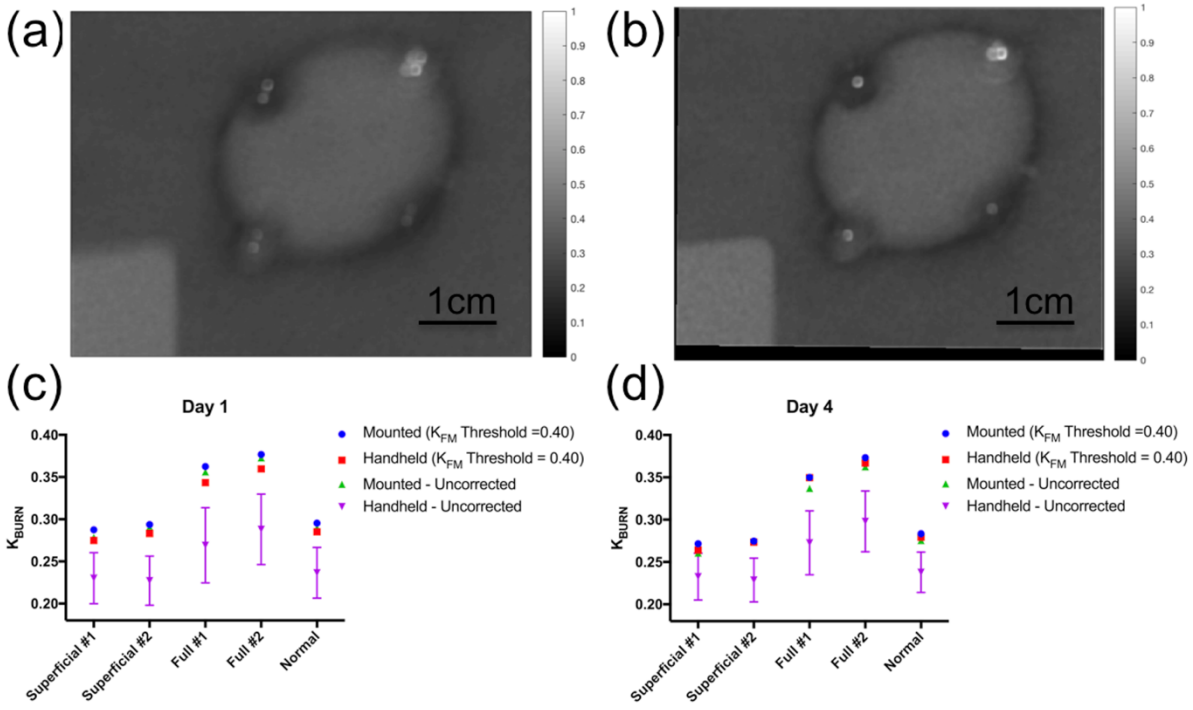

Figure 1.4: Mounted versus handheld speckle contrast of superficial and full thickness burns induced on a porcine model. For both the mounted and handheld data sets, we applied $K_{FM,thres} = 0.40$. (a,b) Average K image of sequence of mounted LSI images of a full-thickness burn wound, (a) without and (b) with use of the FM for alignment and thresholding. Within the image the larger circular region is the burn region, and the smaller four circular region are biopsy points taken over the course of the study. (c) Day 1 K_{BURN} data was obtained at approximately 24 hours post burn. The difference in K_{BURN} between thresholded mounted and handheld data sets was 4%, and the difference between superficial and full thickness burns was 27%. (d) Day 4 K_{BURN} data was acquired 4 days post burn, when the burn wounds have stabilized. The difference in K_{BURN} between thresholded mounted and handheld data sets was 1%, and the difference between superficial and full thickness burns was 32%. The uncorrected handheld data reported K_{BURN} values ~20% lower than handheld with use of the FM.

1.5 Discussion and Conclusion

LSI is a simple, noncontact method for mapping superficial blood flow. We previously used LSI in both pre-clinical and clinical imaging studies, including monitoring of blood flow in a rodent dorsal window chamber model[12–14], pre-clinical imaging of a graded burn wound porcine model, and clinical imaging of pulsed-dye laser treatment on port-wine stain patients[15,21]. Although the system components used in these studies and the associated fields of view varied considerably, each system used mounted setups with a stable platform for imaging.

In a clinical setting, the ease and ability of transportation of a device is expected to increase clinical acceptance and use. A handheld LSI device would enable measurements in settings in which it is not possible to use a mounted or bulkier system, such as in the crowded intensive care units and in portable military or civilian medical units. Previous work was done using a first-generation tablet-based, handheld LSI device, capable of performing non-contact, wide-field measurements.[24] The imaging protocol did not consider quantification of motion artifact or alignment of images collected within a given data set. To mitigate the contributions of motion artifact to measurements of K was achieved only through averaging over 100 raw speckle images to obtain an accurate K value.

Here, we have demonstrated that inclusion of a FM into our imaging field of view and subsequent analysis of measurements from the FM addresses two important aspects that otherwise affect handheld LSI measurements. First, the FM selected has a different K value compared to the silicone phantoms *in vitro* and surrounding tissue *in vivo*. We used the K value of the FM to sort images collected in a sequence in descending order of K_{FM}. This approach allowed us to identify images with the least motion artifact. Second,

following identification of the images with the least motion artifact, we used the FM to align these select images. With the FM in the image FOV, image co-registration was achieved by aligning based on the edges of the FM in each image. Collectively, use of the FM accounted for motion artifact and enabled image alignment.

Previous reports on clinical speckle contrast image registration and correction exist in the literature. Richards *et al.*[14] describe image alignment of the speckle contrast images using rigid translation. They did not require use of a FM because their intraoperative images contained distinct microvascular structure that facilitated image rotation and translation. In speckle contrast images of cutaneous blood flow, distinct architectural landmarks are not always present, so a more generic approach such as use of a FM is required. Mahe *et al.*[15] described use of an opaque material known as Leukotape and correction of speckle flow values using a simple linear relationship. However, with their method, an individual calibration was required for each subject, which limits the utility of this approach as a general motion artifact removal technique. Omarjee *et al*.[9] subsequently studied other materials and identified a bilayer material that they could apply towards calibration-free removal of motion artifact from LSI data. Although their approach appears to decrease the noise associated with motion artifact in LSI measurements, they do not present analysis on how different degrees of motion artifact affect K values. In this work, we chose to use the FM strictly to identify the degree to which raw speckle images are affected by motion artifact, to study how the FM can be used to identify a subset of images with an acceptable degree of motion artifact, and to serve as a guide for automated image alignment and quantification from that subset of images.

Methods for blood flow assessment of burn wounds are able to identify a difference in burn severity.[15] Burn severity is normally assessed by the physician, but assessment is accurate only 60-80% of the time and only once the burn wound has stabilized days after the initial burn.[16-18] The importance of an acute, objective method for distinguishing different burn severities is that the treatment plan will differ depending on the type of burn. Commercial LSI systems are readily available for burn wound measurements, but these systems are expensive and not easily transportable. We showed that our approach of a handheld LSI device with a FM potentially can enable accurate measurements of K with reduced cost and increased portability. Future studies are warranted.

Other possible applications for handheld LSI in a clinical setting include blood flow imaging of the extremities for patients with diabetes[19] or monitoring of peripheral vascular disease[20]. A need also exists for non-invasive blood flow measurements of preterm neonates with potentially abnormal blood flow due to developmental issues.[21] LSI has the potential to provide important diagnostic information for these and other applications. An advantage of LSI is that it is a non-contact, wide-field imaging methodology, unlike currently used point measurement techniques such as laser Doppler flowmetry. The wide-field nature of LSI inherently provides spatial information potentially at video rates. With integration of a graphical user interface (GUI) and tablet-based form factor, our intention was to develop a LSI device that could be used by a non-specialist, such as a member of clinical staff, to facilitate data collection at any time by minimizing barriers to access and use of the device.

Our study has limitations. The current processing time required to sort through each data set and align the images to identify K_{FM} is approximately 30 seconds, and hence is

not a real-time protocol. The severity of this limitation can be mitigated with more efficient software development, perhaps using algorithms written in C. Similarly, real-time image alignment would require revisions made to the software.

In summary, our *in vitro* and *in vivo* data collectively suggest that handheld LSI with use of a FM is feasible and a potentially viable approach for bedside blood-flow monitoring. With incorporation of a FM, we can account for motion artifact and reduce its influence on the data, and we can align images to improve the quantitative accuracy resulting from image averaging.

1.6 Acknowledgements

This material is based upon work supported by the Air Force Office of Scientific Research under award numbers FA9550-17-1-0193, FA9550-14-00340, and FA9550-16-1-0342, which funded development of the handheld LSI technology and phantom testing. Support for the graded burn wound on porcine model experiments were provided by NIH/NIGMS R01GM108634. We also acknowledge support from the Arnold and Mabel Beckman Foundation, the NIH Laser Microbeam and Medical Program Grant P41 EB015890, the NIH funded Institute of Clinical and Translational Science TL1 TR001415 Fellowship to Ben Lertsakdadet, the National Science Foundation Graduate Research Fellowship Program under Grant No. DGE-1321846 to Christian Crouzet, and the Cardiovascular Applied Research and Entrepreneurship Fellowship through the Edwards Lifesciences Center for Advanced Cardiovascular Technology's NIH/NHLBI T32 Training Grant No. 5T32HL116270 to Cody Dunn. The content is solely the responsibility of the authors and does not necessarily represent the official views of the NIGMS, NIBIB or NIH. Any opinions, finding, and conclusions or recommendations expressed in this material are

those of the authors and do not necessarily reflect the views of the United States Air Force. We acknowledge visiting scholars Drs. Yasuyuki Tsunoi and Rajan Arora for their contributions to this study.

CHAPTER 2: Handheld Motion Stabilized Laser Speckle Imaging

2.1 Abstract

Laser speckle imaging (LSI) is a wide-field, noninvasive optical technique that allows researchers and clinicians to quantify blood flow in a variety of applications. However, traditional LSI devices are cart or tripod based mounted systems that are bulky and difficult to maneuver in a clinical setting. We previously showed that the use of a handheld LSI device with the use of a fiducial marker (FM) to account for motion artifact is a viable alternative to mounted systems. Here we incorporated a handheld gimbal stabilizer (HGS) to produce a motion stabilized LSI (msLSI) device to further improve the quality of data acquired in handheld configurations. We validated the LSI device *in vitro* using a flow phantom experiments and *in vivo* using a dorsal skinfold window chamber. For *in vitro* experiments, we quantified the speckle contrast of the FM (K_{FM}) using the mounted data set and tested 80% and 85% of K_{FM} as thresholds for useable images ($K_{FM,Mounted,80\%}$ and $K_{FM,Mounted,85\%}$). Handheld data sets using the msLSI device (stabilized handheld) and handheld data sets without the HGS (handheld) were collected. Using $K_{FM,Mounted,80\%}$ and $K_{FM,Mounted,85\%}$ as the threshold, the number of images above the threshold for stabilized handheld (38 ± 7 and 10 ± 2) was significantly greater ($p=0.0312$) than handheld (16 ± 2 and 4 ± 1). We quantified a region of interest within the flow region (K_{FLOW}), which led to a percent difference of $8.5\% \pm 2.9\%$ and $7.8\% \pm 3.1\%$ between stabilized handheld and handheld configurations at each threshold. For *in vivo* experiments, we quantified the speckle contrast of the window chamber (K_{WC}) using the mounted data set and tested 80% of K_{WC} ($K_{WC,Mounted,80\%}$). Stabilized handheld provided 50 ± 7 images above $K_{WC,Mounted,80\%}$,

while handheld provided only 23 ± 13 images. We quantified the speckle flow index (SFI) of the vessels and the background to obtain signal-to-background ratio (SBR) of the window chamber. Stabilized handheld provided a greater SBR (2.04±0.09) compared to handheld (1.67±0.15). These results display the improved usability of handheld data acquired with an msLSI device.

2.2 Introduction

Laser speckle imaging (LSI) is a wide-field, noninvasive optical technique that allows researchers and clinicians to quantify blood flow in a variety of applications. In a research setting, some applications of LSI include measuring blood flow in the animal brain during externally stimulated conditions [11] , measuring blood flow in a window chamber as a response to therapies [12–14], and measuring blood flow in varying severities of induced burn wounds [15,16]. In a clinical setting, LSI can also provide assistance in assessing medical conditions such as peripheral vascular disease [17], diabetes [18], and burn wounds at the bedside through measured blood flow [19].

The widespread use of LSI in the clinic has been hindered by the bulky form factor of currently available LSI devices such as cart or tripod mounted systems [Pericam PSI System, Perimed AB, Sweden]. They can be cumbersome and difficult to maneuver in a crowded hospital setting, which requires increased portability and convenience. A potential solution for portable clinical blood flow imaging is a handheld LSI device [24]. We have shown that a handheld LSI device enables the collection of meaningful data if issues related to motion artifact are properly addressed [44].

Two concerns of handheld LSI are image misalignment and motion artifact (Fig. 2.1). Figure 2.1 (a) and (b) show examples of these issues when acquiring data during an *in vitro*

flow phantom experiment (Section 2.3.3) and an *in vivo* window chamber measurement (Section 2.3.4). Both of these can be addressed by using a fiducial marker (FM) [44]. Using a FM, we can account for motion artifact by sorting through images to identify frames with the least amount of motion artifact. To account for issues with image misalignment, we can use the fiducial marker to align (co-register) images to produce average blood flow maps, or speckle flow index (SFI) images, which can provide more reliable flow maps that are less sensitive to these motion artifacts.

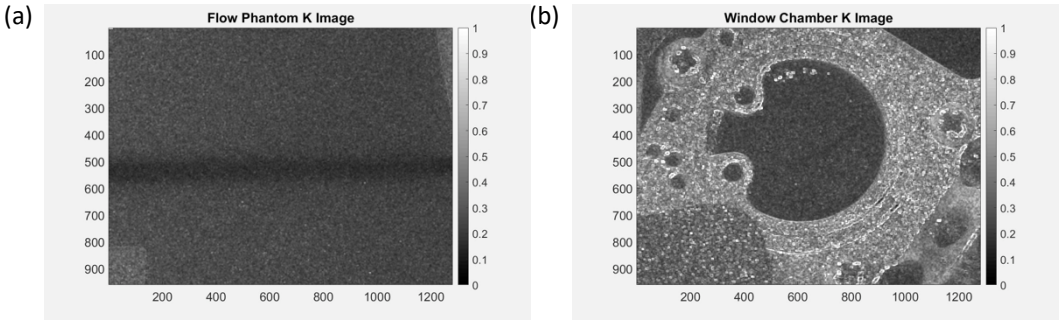

Figure 2.1: Motion artifact during data acquired using LSI device in handheld configuration. A sample data set of K images from an *in vitro* flow phantom measurement (a) and an *in vivo* window chamber measurement (b) are shown. In both cases, the sample translationally shifts within the field of view and K decreases or increases with increasing or decreasing amounts of motion artifact, respectively, present during data acquisition. In (b), the loss of visualization of the blood vessels within the window chamber is due to motion artifact.

In addition to the use of a fiducial marker, we propose that the use of a handheld gimbal stabilizer further reduces motion artifact associated with data acquired in a handheld manner. Handheld gimbal stabilizers (HGS) are commonly used in video recording to reduce vibrations and shakiness when holding cameras. However, HGS have never been paired with LSI systems for measuring blood flow. We hypothesize that pairing a LSI system with a HGS, we can further reduce motion artifact than LSI in a handheld manner.

In this work we show that a handheld gimbal stabilized laser speckle imaging device, which we refer to as our motion stabilized LSI (msLSI) device, reduces motion artifact when acquiring data in a handheld manner. This leads to an increased number of useable frames above our predefined threshold, which was determined from our mounted data sets. We validate the improved motion artifact correction in both *in vitro* flow phantom experiments and *in vivo* dorsal skinfold window chamber measurements.

2.3 Materials and Methods

2.3.1 Motion Stabilized Laser Speckle Imaging Device

The LSI device consisted of an 8-bit, 1.32 megapixel CCD camera (CMLN-13S2M-CS, FLIR Integrated Imaging Solutions, Inc., Richmond, BC, Canada, pixel size = 3.75μm), a variable zoom C-mount lens (Computar C-Mount 13-130mm Varifocal Lens, Computar, Cary, NC), and 809nm near-infrared laser diode (140mW, Ondax Inc., Monrovia, CA). The laser was attached to the camera and lens setup with a custom 3D-printed camera mount. The imaging system acquired 1280 x 960 pixel frames at 15Hz, which resulted in a field of view (FOV) of approximately 140mm x 105mm (4:3 ratio). The imaging system was attached to a HGS (Crane v2 3-Axis Handheld Gimbal Stabilizer, Zhiyun-Tech) to create the msLSI device (Fig. 2.2). The msLSI device was connected to a tablet computer (Surface Pro 2, Microsoft Inc.) via a six-foot-long A-Male to Mini-B USB cable. Data were collected using the FlyCap2 Software (FLIR Integrated Imaging Solutions, Inc., Richmond, BC, Canada) and processed using custom code written in MATLAB (The Mathworks, Natick MA).

Figure 2.2: Motion Stabilized Laser Speckle Imaging (msLSI) Device. Fully-assembled device utilizing a gimbal stabilizer with the laser speckle imaging device.

2.3.2 Fiducial Marker Identification

To test motion artifact reduction, the imaging system was used in a handheld manner both with and without the HGS. The setup for each configuration was comparable in weight to control for potential advantages if one load was lighter. We ensured Nyquist was satisfied at all magnifications with the LSI device. A spatial processing algorithm was used to convert all raw images to speckle contrast images. The spatial processing algorithm utilized a 7x7 pixel sliding window with the relationship $K=\sigma/\langle I\rangle$ calculated for each sliding window position. K is the contrast, σ the standard deviation of the pixel intensities within the window, and $\langle I\rangle$ the mean intensity of the pixels within the window. As previously described in Lertsakdadet et al., a FM made from an 18% grey card, (Neewer, model #10079934) commonly used to correct for white balance in photography, was incorporated into the imaging protocol. We utilized this FM for thresholding and image co-registration. Custom written MATLAB code identified the FM in each frame and quantified the speckle contrast of the fiducial marker (K_{FM}) (Fig. 2.3). Images within each data set

were then sorted based on K_{FM}. Using the mounted LSI data, thresholds of 80% and 85% K_{FM} from a mounted configuration ($K_{FM,Mounted,80\%}$ and $K_{FM,Mounted,85\%}$) were then used to identify the acceptable images from each handheld data set. Custom MATLAB code automatically co-registered these images in each data set to create an average speckle contrast image (Fig. 2.3). Regions of interest within the flow region were selected using the average speckle contrast image (K_{FLOW}).

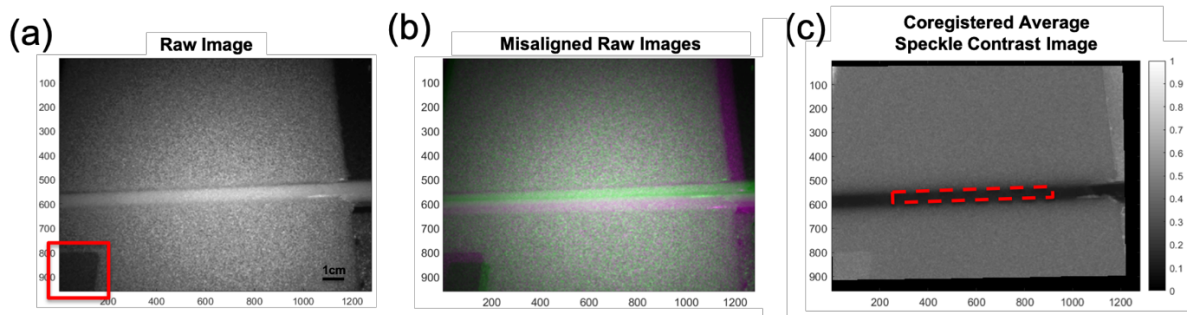

Figure 2.3: Workflow to co-register each speckle contrast image contained within a sequence of images. (a) Representative raw speckle image. The fiducial marker (denoted by red box) in each raw image is identified and the mean speckle contrast value of the marker (K_{FM}) is calculated. (b) False-color image showing degree of misalignment among raw images. Green and purple shading of pixels is used to highlight the fixed and misaligned images, respectively. (c) After identifying the speckle contrast images with K_{FM} above $K_{FM,Mounted,80\%}$ and $K_{FM,Mounted,85\%}$, the misaligned images are aligned and cropped to produce the final co-registered average speckle contrast image. An ROI within the dynamic flow region is selected (in red).

2.3.3 *In Vitro* Flow Phantom Experiment

To test the hypothesis that msLSI performs better than standard handheld LSI, we performed an *in vitro* flow phantom experiment using the LSI device in four configurations: 1) mounted, 2) mounted with gimbal stabilizer (stabilized mounted), 3) handheld, and 4) handheld with gimbal stabilizer (stabilized handheld). The FOV of the device was set to ~140mm x 105mm (4:3 ratio) and the exposure time of the device set to 10ms. We used a solid silicone phantom with a surface-level inclusion flow tube (inner diameter 10mm). The flow medium was a 1% Intralipid solution (Fresenius Kabi, Lake Zurich, IL) that was

infused into the tube using a mechanical pump (NE-1000 Single Syringe Pump, Pump Systems Inc.). The flow speed of the flow medium was changed from 0mm/s to 5mm/s in 1mm/s increments. Sequences of 150 images were acquired with all configurations.

We wanted to compare the differences in stability due to the hardware change of acquiring data with or without the HGS, so after acquiring data with all four configurations, we determined the number of images above $K_{FM,Mounted,80\%}$ and $K_{FM,Mounted,85\%}$ in the handheld and stabilized handheld data sets. Although the number of images above each threshold was different, we used the number of images determined in the stabilized handheld data sets to create the average speckle contrast images for both the handheld and stabilized handheld configurations. This was done to remove biases associated with using differing number of images to create the average speckle contrast image. For handheld and stabilized handheld configurations, multiple users (n = 4) operated the device.

2.3.4 *In Vivo* Dorsal Window Chamber Experiment

As a demonstration, we collected LSI data of the microcirculation from a mouse dorsal window chamber. The animal surgery was carried out according to the protocol outlined in *Moy et al. 2011* and was performed under protocol AUP-17-074 approved by the Institutional Animal Care and Use Committee at University of California, Irvine. The animal was anesthetized using isoflurane (2%, balance oxygen) and the LSI device used to acquire data with each of the four previously mentioned configurations. The window chamber consisted of a 10mm viewing window of the vascular network on the subdermal side.

To account for the smaller features of the window chamber model, the FOV of the LSI device was changed to approximately 20mm x 15mm. An exposure time of 5ms was used to account for the smaller FOV. Sequences of 150 images were acquired with each

configuration. Since each frame in a data sequence may have varying amounts of motion artifact, custom MATLAB code was written to take into account these fluctuations in K and automate identification of the window chamber in each image (Fig. 2.4).

In order to automate identification of the tissue region within the window chamber of each data sequence, we first utilized a scanning quantile to account for the dynamic K images. Using quantiles allows us to scan each image column-wise and row-wise and sort the K of each pixel [45]. In doing so, we can identify the location of the tissue within the window chamber since the K associated with the tissue differs from the K associated with the titanium window chamber (Fig. 2.4a,b). By multiplying the row-wise and column-wise quantile images, we are able to increase the contrast between the tissue and the window chamber (Fig. 2.4c). Since we expected the FM in the window chamber to have a lower K, we were able to identify the window chamber after thresholding the quantiled image (Fig. 2.4d). The resultant threshold image was inverted to create a mask of the window chamber (Fig. 2.4e). A size threshold was applied to remove smaller masked regions that were not the tissue region (Fig. 2.4f). A fill was performed to create a solid mask for blob counting-based identification of a circular region (Fig. 2.4g). The tissue region was identified and a logical mask was created (Fig. 2.4h,i). Using the logical mask, we are able to create a masked K image showing only the tissue region within the window chamber, which will be used for co-registration (Fig. 2.4j).

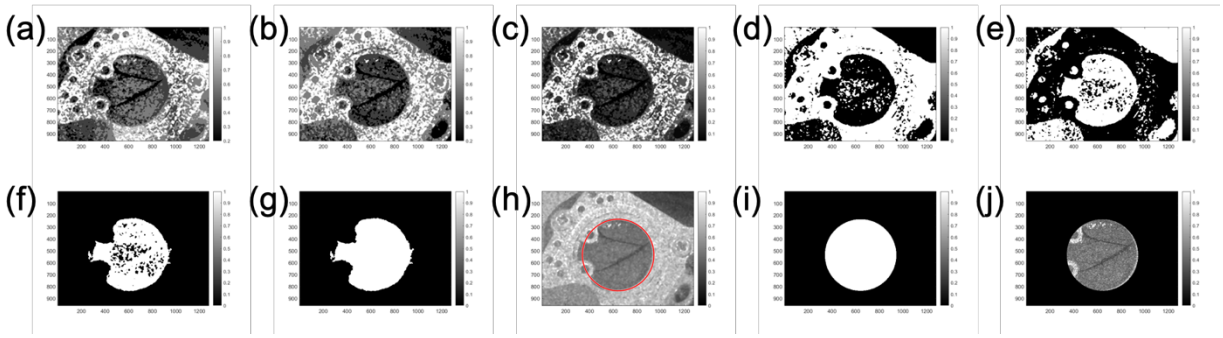

Figure 2.4: Automated identification of mouse dorsal window chamber from raw speckle image sequence. (a) Column-wise quantile K image (b) Row-wise quantile K image (c) Multiplied column-wise and row-wise K image (d) Binarization of multiplied K image (e) Inverted binarized image (f) Feature removal of smaller regions (g) Filled remaining feature (h) Circular geometric identification of tissue within window chamber (i) Create mask using identified circle (j) Mask applied to K image.

For the *in vivo* experiments, the mean speckle contrast value of the window chamber was calculated as the threshold (K_{WC}). We used the mounted data set to determine the 80% threshold of K_{WC} ($K_{WC,Mounted,80\%}$) and applied this threshold to the handheld and stabilized handheld data sets to determine the number of frames whose contrast was above the threshold. These images were used for coregistration and calculation of an average speckle contrast image for the window chamber. This image was then converted into speckle flow index (SFI) images using the simplified speckle imaging equation $SFI = 1/(2*K^2*T)$, where T is the exposure time in seconds and K the contrast value at each pixel [10]. SFI has been shown to correlate linearly with blood flow over the flow speeds observed in the window chamber [10,46]. Lastly, we select an ROI within the vessel and an ROI of the background tissue to quantify the mean SFI value of the signal (vessel) and background, respectively. These mean SFI values are used to quantify the signal-to-background ratio (SBR).

2.3.5 Statistical Analysis

All handheld and stabilized handheld data were treated as paired data since the same users were involved in each group. As such, a Wilcoxon matched-pairs signed rank test was used to test the statistical significance of both the number of images above the 80% threshold and the signal-to-background ratio between handheld and gimbal stabilized data sets. The analysis assumes that the data set is non-parametric, which we assumed due to the small sample size. We considered p-value < 0.05 to be significant, and significance is denoted by * on the relevant figures.

2.4 Results

2.4.1 *In Vitro* Flow Phantom Experiment

Both the mounted and stabilized mounted data sets resulted in all images with K_{FM} above the $K_{FM,Mounted,80\%}$ and $K_{FM,Mounted,85\%}$. The number of images above $K_{FM,Mounted,80\%}$ and $K_{FM,Mounted,85\%}$ was significantly greater in the stabilized handheld compared to handheld data sets (p=0.0312). Using $K_{FM,Mounted,80\%}$, the number of images above the threshold with handheld and stabilized handheld were 16 ± 2 and 38 ± 7, respectively (Fig. 2.5a). Using $K_{FM,Mounted,85\%}$, the number of images above the threshold with handheld and stabilized handheld were 4 ± 1 and 10 ± 2, respectively (Fig. 2.5b). K_{FLOW} was greater in stabilized handheld compared to handheld data sets in all data sets (Fig. 2.5c). The percent difference in K_{FLOW} between the handheld and stabilized handheld data sets across all flow speeds using $K_{FM,Mounted,80\%}$ and $K_{FM,Mounted,85\%}$ were $8.5\% \pm 2.9\%$ and $7.8\% \pm 3.1\%$, respectively.

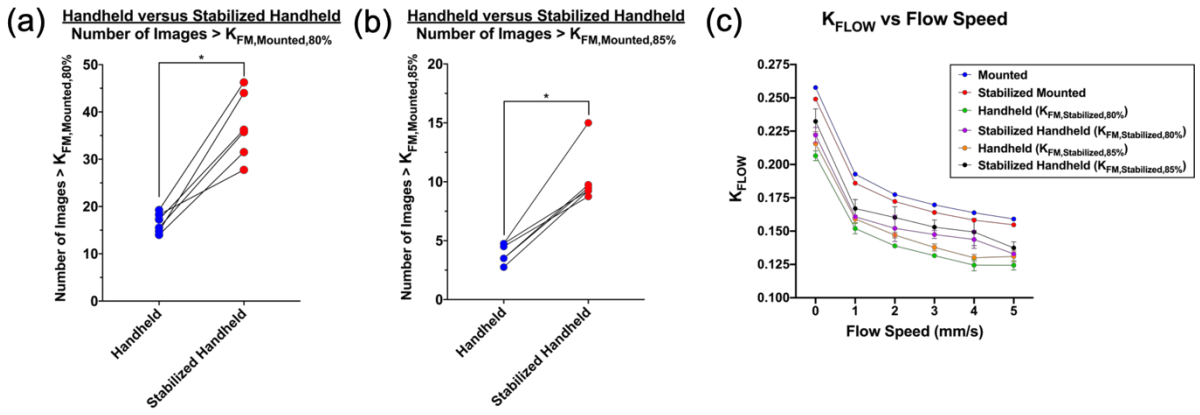

Figure 2.5: A HGS significantly improves the performance of handheld LSI. The mounted speckle contrast of the fiducial marker (K_{FM}) was quantified and used to set an 80% and 85% threshold, $K_{FM,Mounted,80\%}$ and $K_{FM,Mounted,85\%}$, respectively. We then determined the number of images in handheld and stabilized handheld data sets with K_{FM} above these thresholds. (a,b) The number of images above $K_{FM,Mounted,80\%}$ and $K_{FM,Mounted,85\ \%}$ in the stabilized handheld data sets was significantly greater than for the handheld data sets ($p=0.0312$). With mounted and stabilized mounted configurations, the value of K_{FM} in the entire image sequence (150 images) was above 80% K_{FM} (not shown). (c) The speckle contrast within the flow region (K_{FLOW}) of the tissue phantom was greater in stabilized handheld vs handheld at all flow speeds when using both $K_{FM,Mounted,80\%}$ and $K_{FM,Mounted,85\ \%}$, which resulted in a 8.5% $\pm$ 2.9% and 7.8% $\pm$ 3.1% percent differences, respectively.

2.4.2 *In Vivo* Window Chamber Experiment

After identifying the window chamber using the workflow outlined in Figure 2.4, we applied the $K_{WC,Mounted,80\%}$ threshold and quantified the number of images in each data set above our threshold. The number of images above $K_{WC,Mounted,80\%}$ was greater in the stabilized handheld data sets compared to the handheld data sets (Fig. 2.6). Using the msLSI device provided handheld data sets and stabilized handheld data sets provided 23±13 and 50±7 images, respectively (Fig. 2.6a). We coregistered the images based on the window chamber and created an average SFI image for each data set (Fig. 2.6b,c). The SBR of the SFI images were quantified using the SFI value within a ROI of the vessels over the SFI value of the static background. A higher SBR is associated with reduced motion artifact. The SBR in the handheld data sets was 1.67±0.15 compared to 2.04±0.09 in stabilized

handheld data sets (Fig. 2.6d). These resulted in p=0.25.

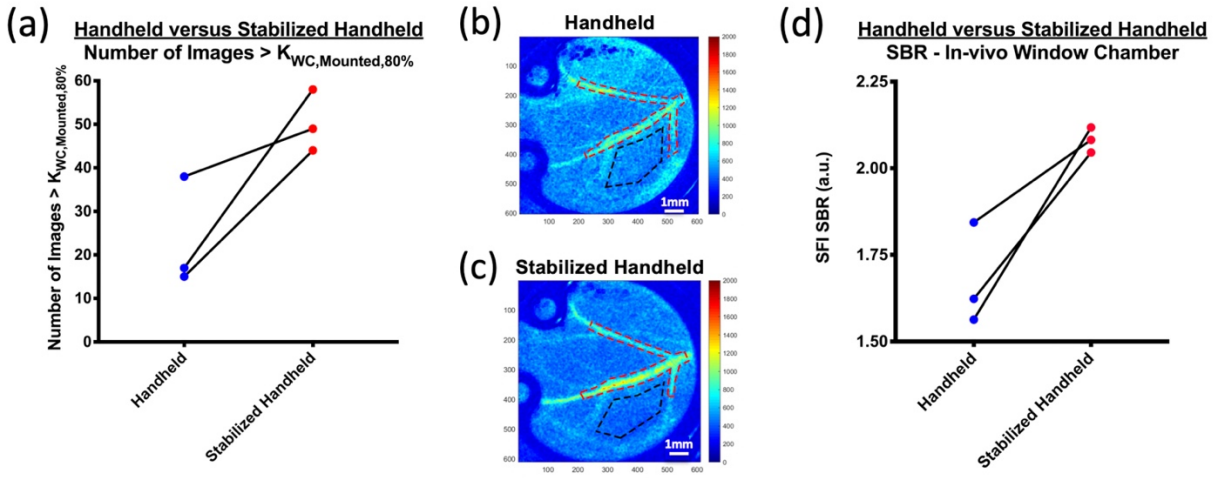

Figure 2.6: Use of a gimbal stabilizer improves the performance of handheld LSI for imaging microvasculature. (a) The number of images above $K_{WC,Mounted,80\%}$ was quantified. The mean and standard deviation of number of images above threshold in the handheld and stabilized handheld data sets were 23±13 and 50±7, respectively (p = 0.25). Sample average SFI images from a single user for handheld (b) and stabilized handheld data (c) sets show that handheld leads to a higher SFI in the background. ROIs of the vessel (red) and background (black) are outlined. The mean and standard deviation of the signal-to-background ratio for handheld and stabilized handheld data sets were 1.67±0.15 and 2.04±0.09, respectively (p=0.25).

2.5 Discussion and Conclusion

LSI can be applied to a wide range of pre-clinical and clinical studies [11–14,21,24,46–48]. However, a portable device is desirable for clinical applications where space is limited. A handheld LSI device is a potential solution for clinical blood flow imaging at the bedside. In our previous study, we showed the viability of using LSI in a handheld manner [24,44]. Other handheld LSI devices have been created, but the primary application space is for retinal blood flow imaging [25]. They also state that they acquire data in a "stabilized" configuration; however, the stabilized method they refer to is attaching their handheld LSI device to a rigid mount on a table. Our stabilized approach is novel in that we are using a HGS in both a handheld configuration and a mounted configuration. By incorporating a HGS to a LSI

device, we have shown that msLSI can further reduce motion artifact when acquiring handheld LSI.

Stabilized handheld data sets provided significantly more frames above $K_{FM,Mounted,80\%}$ and $K_{FM,Mounted,85\%}$ thresholds compared to handheld only. Since all data sets contained the same number of images, stabilized handheld data resulted in a higher rate of useable frames. This can reduce imaging times by allowing a lower number of frames acquired using stabilized handheld but resulting in the same number of useable frames as handheld. By reducing data acquisition times and motion artifact, stabilized handheld becomes a more viable option for clinical use compared to bulky conventional LSI devices.

An additional consideration for clinical blood flow imaging is the desired FOV for specific applications. Hence, LSI devices used in clinical studies have a large range of FOV. The Pericam PSI device provided a 120mm x 120mm FOV when imaging scald burn in patients, while a LSI dermascope provided a 5mm x 3.75mm while measuring skin lesions [9,14]. Using a smaller FOV amplifies motion artifact making it less feasible for non-contact handheld LSI. However, when we reduced the FOV of the msLSI device from 140mm x 105mm to 20mm x 15 mm we were able to show there is an improved SNR in the stabilized handheld configuration.

Although we have shown that msLSI is a viable alternative to conventional LSI systems for clinical use, there are some limitations to consider. By incorporating a HGS to a handheld LSI device, we increase both overall cost and weight of the system. The added weight may make it more difficult to steadily operate. However, we plan to address this in future generations of the device by miniaturizing the LSI device and HGS. Another limitation of handheld LSI is the inherent motion due to using the device in a handheld

configuration, which will decrease K in an entire image. We plan to account for this by continuing to utilize a FM in the imaging protocol.

In summary, we further displayed the potential for handheld LSI by testing a msLSI device. We validated the improved stability and reduced motion artifact in both *in vitro* and *in vivo* experiments with multiple users. We varied the FOV of the device and showed that msLSI can provide useable blood flow maps even at smaller FOV where motion artifact is amplified. The msLSI is a viable alternative to conventional LSI devices for a variety of clinical applications. Future studies will attempt to use the msLSI device for clinical blood flow measurements.

2.6 Acknowledgements

We acknowledge support from the Arnold and Mabel Beckman Foundation, the NIH Laser Microbeam and Medical Program Grant P41 EB015890, the NIH funded Institute of Clinical and Translational Science TL1 TR001415 Fellowship to Ben Lertsakdadet, the National Science Foundation Graduate Research Fellowship Program under Grant No. DGE-1321846 to Christian Crouzet, and the Cardiovascular Applied Research and Entrepreneurship Fellowship through the Edwards Lifesciences Center for Advanced Cardiovascular Technology's NIH/NHLBI T32 Training Grant No. 5T32HL116270 to Cody Dunn. The content is solely the responsibility of the authors and does not necessarily represent the official views of the NIGMS, NIBIB or NIH.

CHAPTER 3: Optical Property Corrected Flow

3.1 Abstract

Early and accurate assessment of burn wound severity is important for both identifying the path of treatment and minimizing complications during recovery. In the case of more severe burn wounds, such as deep partial thickness and full thickness burns, debridement of dead tissue and application of a skin graft is necessary. Current methods for assessing burn wound severity rely on clinical examination, which are subjective. The use of non-invasive imaging modalities can provide an objective method for assessing burn wound severity. Laser Speckle Imaging (LSI) is one such imaging modality that provides wide-field blood flow quantification. However, due to the dynamic nature of burn wounds in the first 48-72 hours, optical property changes associated with these wounds may lead to inaccuracies in the measured blood flow. By measuring these optical property changes with Spatial Frequency Domain Imaging (SFDI) at each time point and combining this information with LSI, we can calculate a dynamically corrected characterized diffusion, $D_{B,dyn,corrected}$, value that takes into account the changing optical properties in the burn wound. In addition, we calculated a characterized D_B value using pre-burn optical properties at all time points, $D_{B,stat,corrected}$, and another characterized D_B value using assumed optical properties, $D_{B,uncorrected}$. We used a varying-burn depth and varying-depth of debridement porcine burn model in an attempt to identify a $D_{B,dyn,corrected}$ value that would distinguish adequately debrided wound beds for successful vs failed grafts. We compared $D_{B,dyn,corrected}$ to $D_{B,stat,corrected}$ and $D_{B,uncorrected}$ at pre- and post-burn on Day -4 and pre- and post-debridement on Day 0. We showed that $D_{B,dyn,corrected}$ and $D_{B,uncorrected}$ differed by up to 47.6% and $D_{B,dyn,corrected}$ and $D_{B,stat,corrected}$ differed by up to 19.6%. Thus, correcting

for optical property changes in dynamic burn wounds can greatly improve the accuracy of LSI measurements. However, we were unable to determine a threshold value for $D_{B,dyn,corrected}$ to distinguish successful vs failed grafts.

3.2 Introduction

American Burn Association approximates 450,000 burn injuries occur in the United States annually[26]. Current clinical protocol for assessing these burn wounds are based on visual observations by an experienced surgeon, which can be subjective[27–29]. Burn wounds can be classified into superficial, partial, deep partial, and full thickness burns. Superficial burn wounds are minor and will heal on their own, whereas full thickness burns require surgical intervention[15]. Partial thickness burns may transform into superficial thickness or deep partial thickness burns, making them more difficult to properly assess and treat. The dynamic nature of burn wounds within the first 48-72 hours makes them extremely difficult to diagnose accurately. However, early and accurate assessment of burn wounds is vital for determining the path of treatment and outcome of the wound[31–33].

Surgical intervention to treat deeper thickness burns requires debridement of the necrotic tissue in preparing the wound bed for application of a meshed split thickness skin graft (mSTSG)[15]. However, it can be difficult to determine how much debridement is considered adequate. We set out to determine the adequate depths of debridement associated with varying burn severities to provide a successful graft. Non-invasive imaging modalities were utilized in order to correlate outcome with quantifiable metrics provided by each modality.

Laser Doppler Imaging (LDI) has been the gold standard modality for quantifying blood perfusion in burn wounds[49–51]. LDI measures the Doppler shift of the detected light

due to scattering by red blood cells (RBC)[50,52,53]. LDI is desirable in that it is a non-contact method, but it is plagued by long measurement times and high costs[49].

Laser Speckle Imaging (LSI) is another optical technique for measuring blood perfusion. LSI uses diffuse laser light to illuminate the entire sample instead of the laser scanning method used in LDI[5,15,16,21,44,47]. LSI measures the fluctuation in the intensity of the reflected light in a single snapshot[7]. Millet et al. also showed excellent correlation between the measured blood perfusion by LSI and LDI across a wide range of human skin perfusion values[54]. Hence, LSI can address the limitations of LDI in providing comparable blood perfusion information with greater temporal resolution. Both LSI and LDI have shown promise in improving upon clinical assessment of burn wounds[15,16,55]. In addition, the perfusion units of LSI, in Speckle Flow Index (SFI), have been shown to correlate linearly with blood flow rates found in tissue[10].

Although studies have shown that blood perfusion is an adequate method for assessing burn wounds, they do not take into account the structural changes that occur. A non-contact imaging modality capable of quantifying these structural changes is Spatial Frequency Domain Imaging (SFDI). SFDI is an imaging technique that provides optical properties of tissue (reduced scattering coefficient, μ_s', and absorption coefficient , μ_a) along with oxy- and deoxy-hemoglobin information[34–39]. Ponticorvo et al. used μ_s' from SFDI and perfusion units from LSI to categorize burns [30]. They showed that at 24 hours post-burn, LSI provided a sensitivity and specificity of 66% and 90%, respectively. At 72 hours, sensitivity improved to 100%, but specificity decreased to 58%. Whereas, SFDI provided a sensitivity and specificity of 93% and 74% at 24 hours, and 83% and 90% at 72 hours.

LSI is a relative blood perfusion method, which does not take into account changes in tissue optical properties. We hypothesize that by utilizing SFDI to measure optical property of the burn wounds, we can improve the accuracy of the perfusion information measured by LSI. Here, we use LSI and SFDI to measure burn wounds in a variable-burn depth and variable-debridement depth porcine burn wound model. In this work, we attempt to quantify the error in LSI measured perfusion units when (1) the dynamic optical properties are determined and used to correct perfusion units, (2) the pre-burn optical properties are used to correct perfusion units, and (3) commonly assumed optical properties are used to correct perfusion units. In addition, we attempted to use LSI, with and without SFDI information, to correlate perfusion measurements immediately post-debridement with successful vs failed outcome of varying burn severity and debridement depths.

3.3 Materials and Methods

3.3.1 Spatial Frequency Domain Imaging Device

The Spatial Frequency Domain Imaging (SFDI) device (ReflectRS, Modulated Imaging, Inc., Irvine, CA) consisted of an imaging head mounted to a mobile cart with an articulating arm. The device provides a FOV of 20cm x 15cm from a height of 32cm from the sample. Images were acquired using the MI Acquire V1.34.00 software and the device was set to acquire 3 data sets of each sample. Each data set consisted of 8 wavelengths from 471nm – 851nm with 5 sinusoidal spatial frequencies, evenly spaced between 0 mm^{-1} and 0.2mm^{-1}. A planar reflectance image was also acquired for each data set. The resulting data sets were used to produce the reduced scattering coefficient (μ_s') and absorption coefficient (μ_a) images used for this study (Fig. 3.1). We selected a region of interest (ROI)

using the μ_s' and μ_a images for each treatment site (Fig. 3.1). We quantified the mean μ_s' and μ_a within these ROIs using an interpolation for 808nm to correspond with the laser wavelength used in the LSI device (Fig. 3.1). All mean optical properties quantified for each burn treatment at the pre- and post-burn and pre- and post-debridement time points can be found in the Appendix.

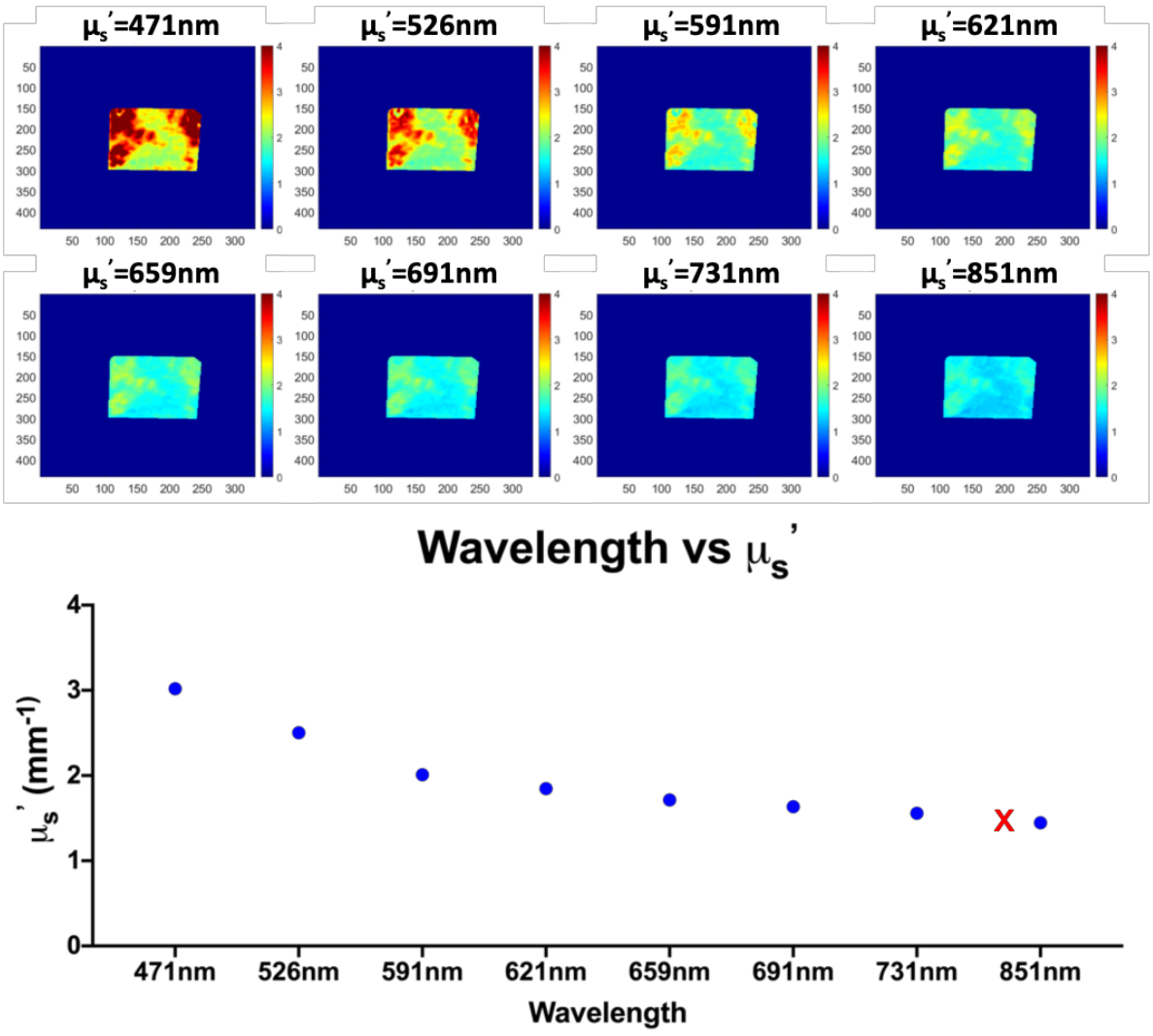

Figure 3.1: Sample data set of wavelength vs μ_s' quantified using the mean of the ROI. Interpolation for 808nm was performed to determine the $\mu_s'_{808nm}$ (red 'x').

3.3.2 Laser Speckle Imaging Device

The Laser Speckle Imaging (LSI) system used in this study consisted of an imaging head mounted to mobile cart with an articulating arm. The imaging head consisted of an 8-bit, 1.32 megapixel CCD camera (CMLN-13S2M-CS, FLIR Integrated Imaging Solutions, Inc., Richmond, BC, Canada), a variable zoom C-mount lens (Computar C-Mount 13-130mm Varifocal Lens, Computar), and 808nm near-infrared laser diode (140mW, Ondax Inc., Monrovia, CA). A 785nm longpass filter was placed in front of the CCD sensor to allow data acquisition with room lights. A 750nm-850nm near-infrared linear polarizer (Edmund Optics) was placed in front of the variable zoom lens in order to remove specular reflectance on the surface of the sample. The device provided a FOV of approximately 14cm x 10.5cm at 35cm away from the sample. Each data set contained 150 raw images acquired at 15Hz. All raw images were converted into speckle contrast (K) images using a 7 x 7 sliding window and the relationship of $K = \sigma/\langle I \rangle$, where σ is the standard deviation and $\langle I \rangle$ is the mean intensity of all pixels within the window. All speckle contrast images from each data set were used to create an average speckle contrast image. The speckle contrast images were also converted in speckle flow index (SFI) images to show relative blood flow, using the relationship of $SFI = 1/2TK^2$, where T is the exposure time in seconds. SFI is a measure of arbitrary units (a.u.). A ROI comparable to the ones selected for the μ_s' and μ_a was selected using the average speckle contrast image (Fig. 3.2). We quantified the mean K and SFI within the ROI.

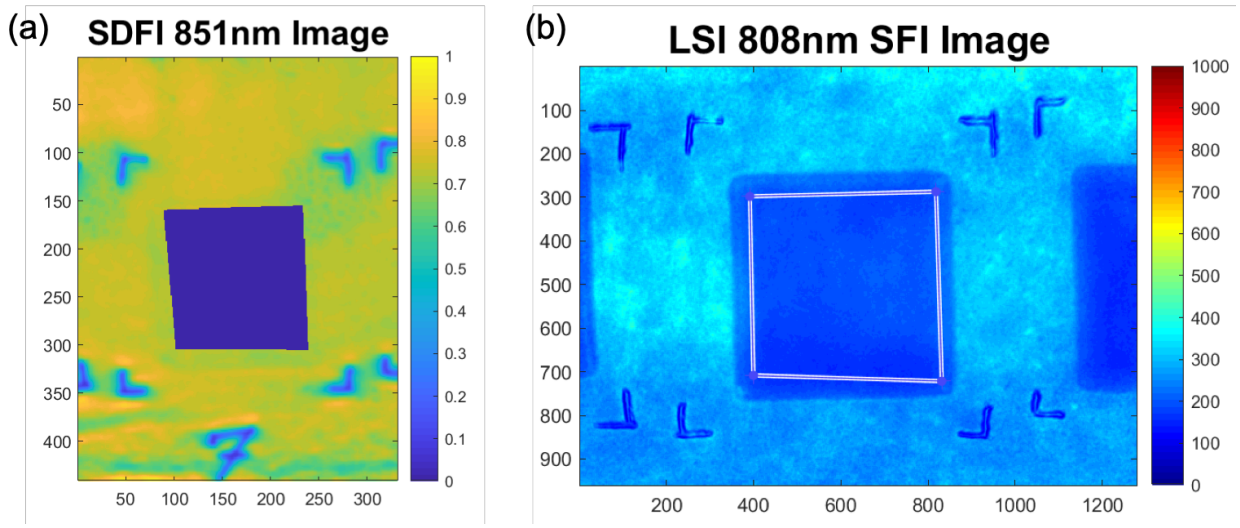

Figure 3.2: SFDI guided LSI ROI selection. (a) A planar reflectance image at 851nm is masked using a selected ROI. This masked SFDI image is used to guide LSI ROI selection (b).

3.3.3 Porcine burn model with varying-burn depth and varying-depth of debridement

All experiments were carried out under an US Army Institute for Surgical Research approved IACUC protocol. Animal research was conducted in compliance with the Animal Welfare Act, the implementing Animal Welfare Regulations, and the principles of the Guide for the Care and Use of Laboratory Animals, National Research Council. The burn treatments varied in severity of burns and depths of debridement (Table 3.1). The severity of the burn was based upon contact time of the burn tool. Burn treatments were randomized and induced on the dorsal side of each pig. Each pig received 10 burn treatments varying from no burn to full thickness burns. The burn tool used was a 5cm x 5cm brass burn tool with active temperature control[56]. Figure 3.3 outlines the timeline of the burn treatment and imaging protocol. LSI and SFDI data was acquired pre- and post-burn on Day -4 of the study. On Day 0 of the study, debridement of the wound bed was performed. The depths of debridement varied from 0.030 inches to 0.120 inches. After

post-debridement imaging was performed, and a meshed split thickness skin graft (mSTSG) was applied to the debrided wound bed. The treatment site is then bandaged in between imaging timepoints to minimize contamination and infection from external sources.

In addition to the 10 burn treatments, 2 control sites were located adjacent to the first and last burn treatments for each pig. LSI and SFDI data was acquired pre- and post-debridement on Day 0 and additionally on Days 3, 7, 10, and 14. A total of 8 pigs were included in this study resulting in LSI and SFDI data on 80 experimental and 16 control sites for post processing and data analysis. The time points of interest for this study were Day -4 pre- and post-burn and Day 0 pre- and post-debridement.

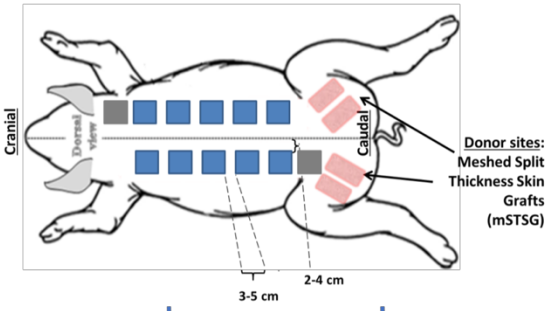

Day – 4	Day 0	Day 3	Day 7	Day 10	Day 14
• Induce Burn • SFDI and LSI imaging pre and post-burn	• Perform Debridement • SFDI and LSI imaging pre and post-debridement • Apply mSTSG	• SFDI and LSI imaging	• SFDI and LSI imaging	• SFDI and LSI imaging	• SFDI and LSI imaging

Figure 3.3: Porcine model burn treatment diagram with timeline for burn treatment and SFDI and LSI imaging.

Table 3.1 Burn treatments varied in both burn severity and depth of debridement. Desired burn depth was determined by contact time of the burn tool onto tissue. Depths of debridement listed are associated with each burn depth.			
Burn Severity (Contact Time)	**Depth of Debridement (inches)**		
Partial Thickness – 6s	0.030”	0.060”	
Partial Thickness – 9s	0.030”	0.060”	0.090”
Deep Partial Thickness – 12s	0.030”	0.060”	0.090”
Full Thickness – 15s	0.060”	0.090”	0.120”
No Burn	0.090”		

3.3.4 Optical Property Corrected Flow

Using the relevant equations from *Mazhar et al.* we were able to observe the effects of changing optical properties on resultant contrast, K[57]. We use the following correlation diffusion equation used to quantify intensity fluctuations in LSI measurements:[57]

$$K^2 = \frac{\frac{2}{T}\int_0^T \beta G_1^2(\tau)\left(1-{}^{\tau}/_{T}\right)d\tau}{G_1^2(\tau=0)} \qquad \text{(Eq. 3.1)}$$

$G_1(\tau)$ is the electric field temporal autocorrelation function, which is related to the intensity autocorrelation function, $G_2(\tau)$, through the Siegert relationship:[6,57]

$$g_2(\tau) = 1 + |g_1(\tau)|^2 \qquad \text{(Eq. 3.2)}$$

The correlation diffusion equation used to model $G_1(\tau)$ in turbid media allows us to associate optical property influence on the resultant speckle contrast (K):[57]

$$\nabla^2 G_1(\tau) - \mu_{eff} G_1(\tau) = q \qquad \text{(Eq. 3.3)}$$

q is the source, μ_{eff} is the effective optical properties, which can be obtained using:

$$\mu_{eff} = [3\mu_{a,dyn}\mu_{tr}]^{1/2} \qquad \text{(Eq. 3.4)}$$

Here, μ_{tr} is the total attenuation coefficient defined by $\mu_{tr} = (\mu_a + \mu_s')$, and $\mu_{a,dyn}$ is the dynamic absorption term defined by:

$$\mu_{a,dyn} \rightarrow \mu_a + \frac{1}{3}\mu_s{}' k_o^2 \langle \Delta r^2(\tau) \rangle$$

(Eq. 3.5)

In $\mu_{a,dyn}$, k_o is the wave number of propagating photons, defined by $k_o = \frac{2\pi n}{\lambda}$, and $\langle \Delta r^2(\tau) \rangle$ is the mean square displacement of dynamic scattering particles. Assuming Brownian motion, $\langle \Delta r^2(\tau) \rangle = 6D_B$, where D_B is the Brownian diffusion coefficient. G_1 becomes:[57]

$$G_1(\tau) = \frac{3P_0 A \frac{\mu_s'}{\mu_{tr}}}{\left(\frac{\mu_{eff}}{\mu_{tr}}+1\right)\left(\frac{\mu_{eff}}{\mu_{tr}}+3A\right)} \quad \text{(Eq. 3.6)}$$

P_0 is the incident optical power and A is a constant dependent upon the boundary conditions. A is defined as:

$$A = \frac{1-R_{eff}}{2(1+R_{eff})};\ R_{eff} \approx 0.0636n + 0.668 + \frac{0.710}{n} + \frac{1.440}{n^2} \quad \text{(Eq. 3.7)}$$

Where R_{eff} is the effective reflection coefficient and n is the index of refraction of the turbid media.

For each of the treatment sites, we used the above equations to create a look up table for K using a range of D_B from 10^{-8} to 10^{-4} and the mean μ_s' and μ_a values from the SFDI images. We then used the mean K value obtained from our ROIs within each treatment site and performed an interpolation using the look up table to determine a dynamically corrected characterized D_B associated to the wound, $D_{B,dyn,corrected}$. This term is considered *dynamic* because the optical properties used for correction were updated at each time point. We consider this term our *characterized* diffusion coefficient because it is representative of the tissue being sampled and is not an absolute measurement of diffusion. In order to obtain an absolute measurement of diffusion, we would need to quantify the hemoglobin saturation and blood volume fraction of the tissue sampled.

Unfortunately, we do not currently have the resolution to distinguish these values. In addition to $D_{B,dyn,corrected}$, we used only the pre-burn optical properties to determine the corrected D_B at all time point, which we refer to as the statically corrected characterized D_B, or $D_{B,stat,corrected}$. Lastly, to compare a condition where optical properties are not measured and must be assumed, we used μ_s'=1mm^{-1} and μ_a=0.01mm^{-1} to create an additional look up table to determine an uncorrected characterized D_B, $D_{B,uncorrected}$. The values of $D_{B,dyn,corrected}$, $D_{B,stat,corrected}$, and $D_{B,uncorrected}$ were used to convey the potential errors associated with assumed optical properties and to calculate the error between using dynamic, static, and uncorrected optical properties in determining characterized D_B.

3.3.5 Statistical Test

A linear regression fit was used to assess each data set to determine the line-of-best-fit. The x-intercept was forced to 50 SFI (a.u.) as this is representative of the condition in which K = 0, in which there is no movement. The slopes of each data sets were compared in Prism 8 (GraphPad Software, Inc.) using the method outlined in Ref [58,59]. The results of this analysis tested the slopes of each data set against the null that the slopes were the same for all data sets. A p-value < 0.05 indicated statistically significant differences in slopes.

3.4 Results

Figure 3.4 shows $D_{B,dyn,corrected}$, which used pre-burn μ_s' and μ_a values from pre-burn SFDI measurements, with respect to the measured SFI values obtained from the LSI device. The $D_{B,uncorrected}$, which used used μ_s'=1mm^{-1} and μ_a=0.01mm^{-1} as the optical property values for quantifying D_B, was plotted in comparison. The slopes of the linear regression fit of each data set were significantly different ($p < 0.0001$). The mean percent error between pre-burn $D_{B,dyn,corrected}$ and $D_{B,uncorrected}$ individual values was -47.6%. The $D_{B,uncorrected}$ over estimated D_B values compared to $D_{B,dyn,corrected}$, hence the negative percent error. The mean μ_s' and μ_a measured at the pre-burn time point with SFDI were 1.34mm^{-1} and 0.0043mm^{-1}, respectively.

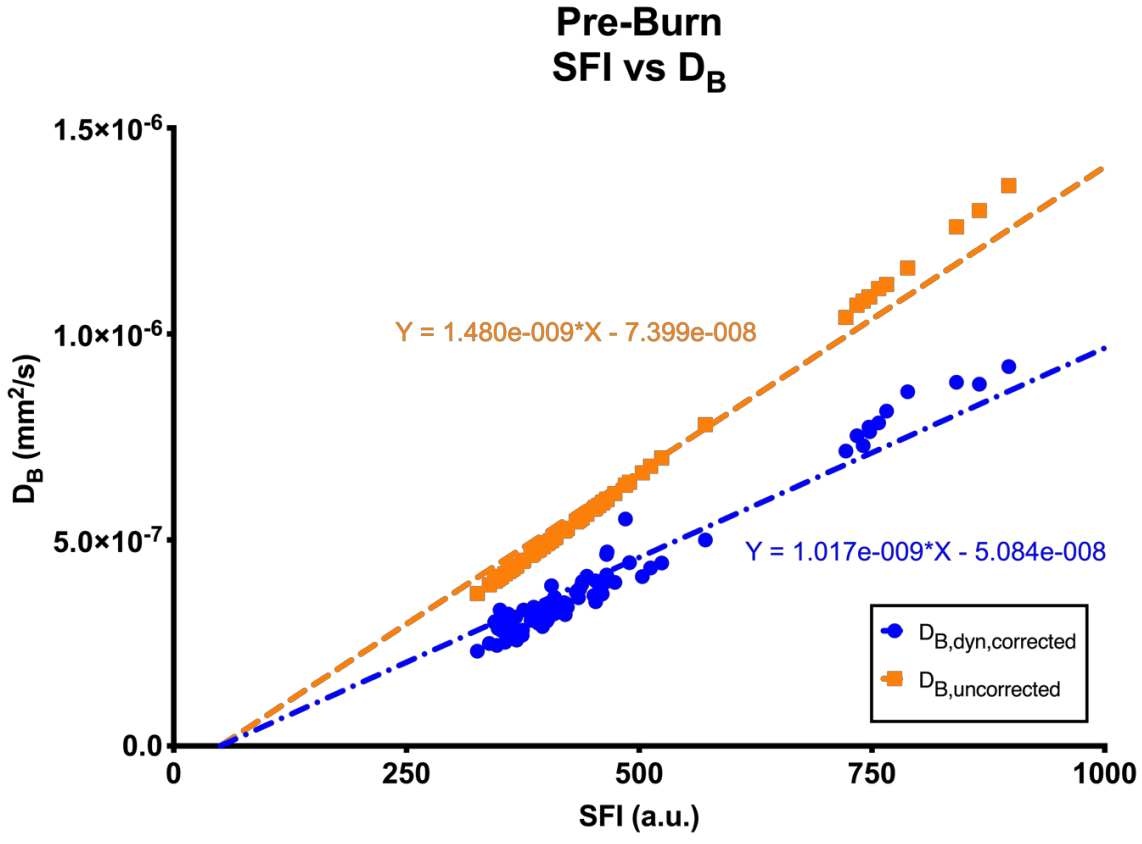

Figure 3.4: Pre-burn SFI vs $D_{B,dyn,corrected}$ and $D_{B,uncorrected}$. The mean percent error between pre-burn $D_{B,dyn,corrected}$ and $D_{B,uncorrected}$ was significantly different with a mean percent error of -47.6%.

Figure 3.5 shows $D_{B,dyn,corrected}$, which used post-burn μ_s' and μ_a values from post-burn SFDI measurements, with respect to the measured SFI values obtained from the LSI device. The $D_{B,stat,corrected}$, which used pre-burn μ_s' and μ_a from SFDI measurements , and $D_{B,uncorrected}$, which used μ_s'=1mm^{-1} and μ_a=0.01mm^{-1}, were plotted in comparison. The slopes of the linear regression fit of each data set were significantly different ($p < 0.0001$). The mean percent error between post-burn $D_{B,dyn,corrected}$ and $D_{B,stat,corrected}$ individual values was 6.89%. $D_{B,stat,corrected}$ underestimated D_B. The mean μ_s' and μ_a measured post-burn were 1.44mm^{-1} and 0.0056mm^{-1}, respectively. The mean percent error between $D_{B,dyn,corrected}$ and $D_{B,uncorrected}$ at the post-burn time point was -40.1%. $D_{B,uncorrected}$ overestimated D_B.

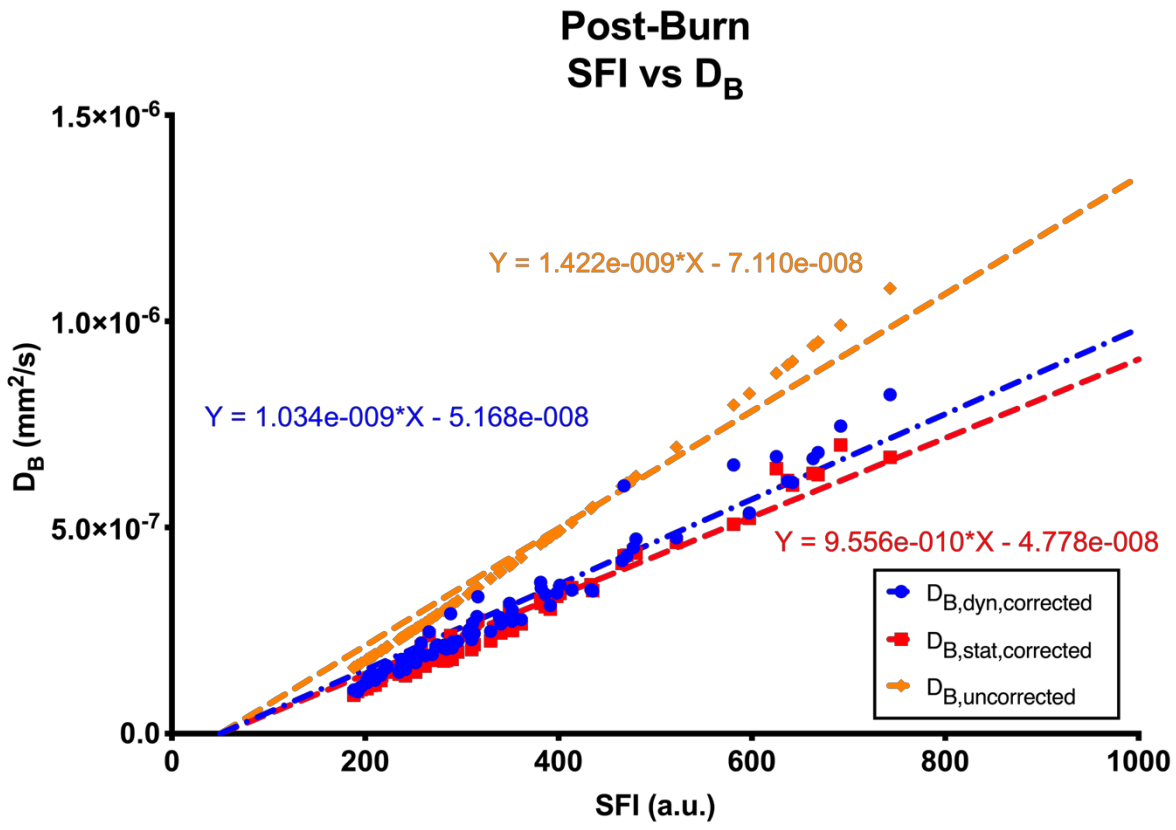

Figure 3.5: Post-burn SFI vs $D_{B,dyn,corrected}$ and $D_{B,stat,corrected}$ and $D_{B,uncorrected}$. Post-burn $D_{B,dyn,corrected}$ and $D_{B,stat,corrected}$ was highly correlated with a mean percent error 6.89%. However, the mean percent error between post-burn $D_{B,dyn,corrected}$ and $D_{B,uncorrected}$ was -40.1%.

Figure 3.6 shows $D_{B,dyn,corrected}$, which used pre-debridement μ_s' and μ_a values from pre-debridement SFDI measurements, with respect to the measured SFI values obtained from the LSI device. The $D_{B,stat,corrected}$, which used pre-burn μ_s' and μ_a from SFDI measurements , and $D_{B,uncorrected}$, which used μ_s'=1mm^{-1} and μ_a=0.01mm^{-1}, were plotted in comparison. The slopes of the linear regression fit of each data set were significantly different ($p < 0.0001$). The mean percent error between pre-debridement $D_{B,dyn,corrected}$ and $D_{B,stat,corrected}$ individual values was 19.3%. The mean μ_s' and μ_a measured pre-debridement were 1.45mm^{-1} and 0.0093mm^{-1}, respectively. The mean percent error between $D_{B,dyn,corrected}$ and $D_{B,uncorrected}$ at the post-burn time point was -21.1%.

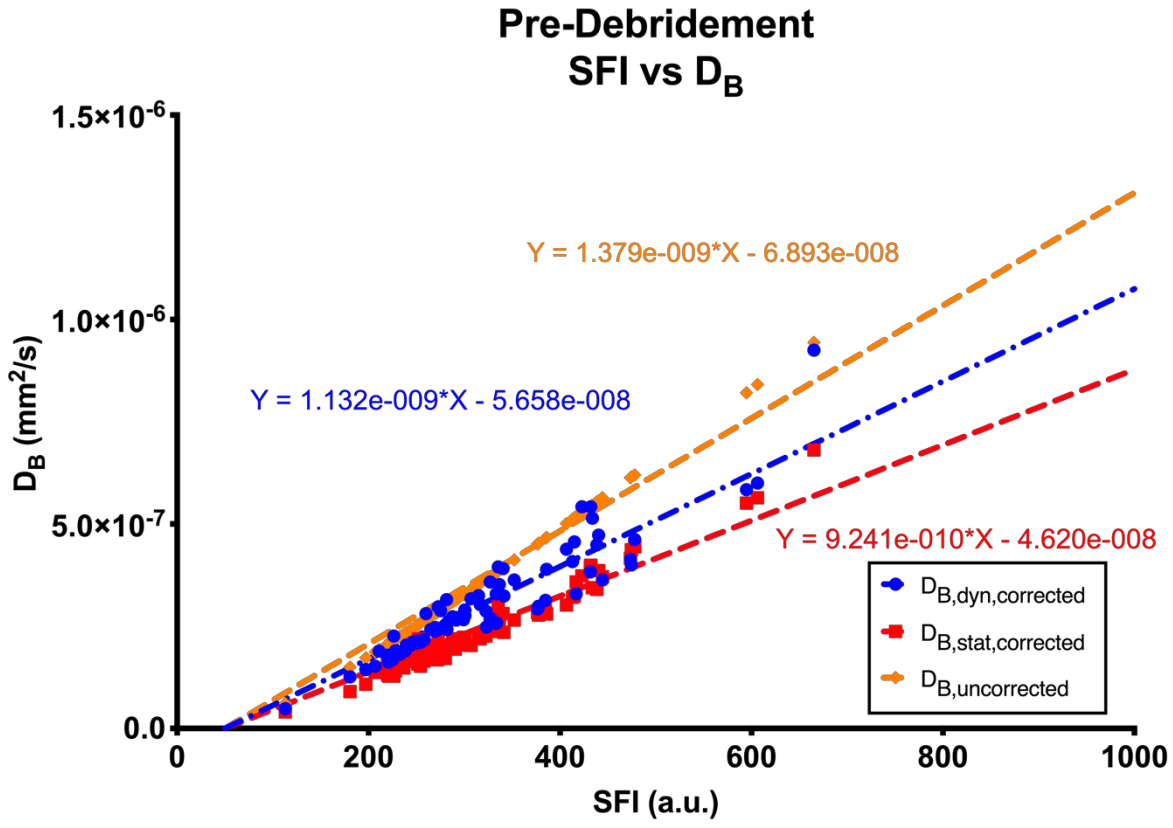

Figure 3.6. Pre-debridement SFI vs $D_{B,dyn,corrected}$ and $D_{B,stat,corrected}$ and $D_{B,uncorrected}$. The mean percent error between pre-debridement $D_{B,dyn,corrected}$ and $D_{B,stat,corrected}$ was 19.3%, whereas the mean percent error between post-burn $D_{B,dyn,corrected}$ and $D_{B,uncorrected}$ was -21.1%.

Figure 3.7 shows $D_{B,dyn,corrected}$, which used post-debridement μ_s' and μ_a values from post-debridement SFDI measurements, with respect to the measured SFI values obtained from the LSI device. The $D_{B,stat,corrected}$, which used pre-burn μ_s' and μ_a from SFDI measurements , and $D_{B,uncorrected}$, which used μ_s'=1mm^{-1} and μ_a=0.01mm^{-1}, were plotted in comparison. The slopes of the linear regression fit of each data set were significantly different ($p < 0.0001$). The mean percent error between post-debridement $D_{B,dyn,corrected}$ and $D_{B,stat,corrected}$ individual values was 19.6%. The mean μ_s' and μ_a measured pre-debridement were 1.42mm^{-1} and 0.0097mm^{-1}, respectively. The mean percent error between $D_{B,dyn,corrected}$ and $D_{B,uncorrected}$ at the post-burn time point was -16.7%.

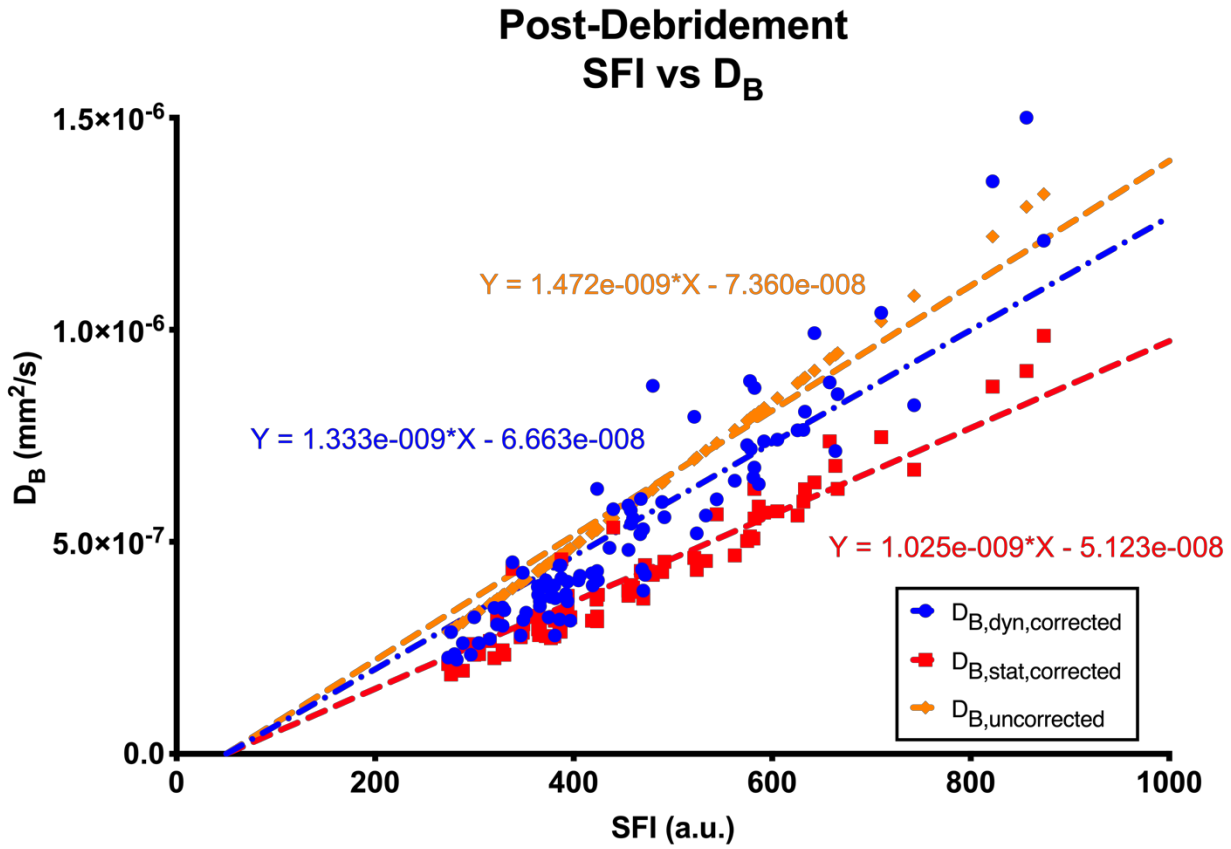

Figure 3.7: Post-debridement SFI vs $D_{B,dyn,corrected}$ and $D_{B,stat,corrected}$ and $D_{B,uncorrected}$. The mean percent error between post-debridement $D_{B,dyn,corrected}$ and $D_{B,stat,corrected}$ was 19.6%, whereas the mean percent error between post-burn $D_{B,dyn,corrected}$ and $D_{B,uncorrected}$ was -16.7%.

We also compared $D_{B,dyn,corrected}$ values at the pre- and post-debridement time points with respect to the burn treatments received for each site (Fig 3.8). An overall increase in $D_{B,dyn,corrected}$ post-debridement was observed (mean percent increase of 115% from pre-debridement) (Fig 3.8a,b). The mean percent error post-debridement of successful grafts and failed grafts were 121% and 76%, respectively (Fig 3.8c). However, the results were inconclusive in determining a threshold for D_B values associated to failed vs successful grafts at the post-debridement time point as seen in the receiver operating characteristic (ROC) curve in Figure 3.8d. The ROC curve showed 85% sensitivity paired with 40% specificity.

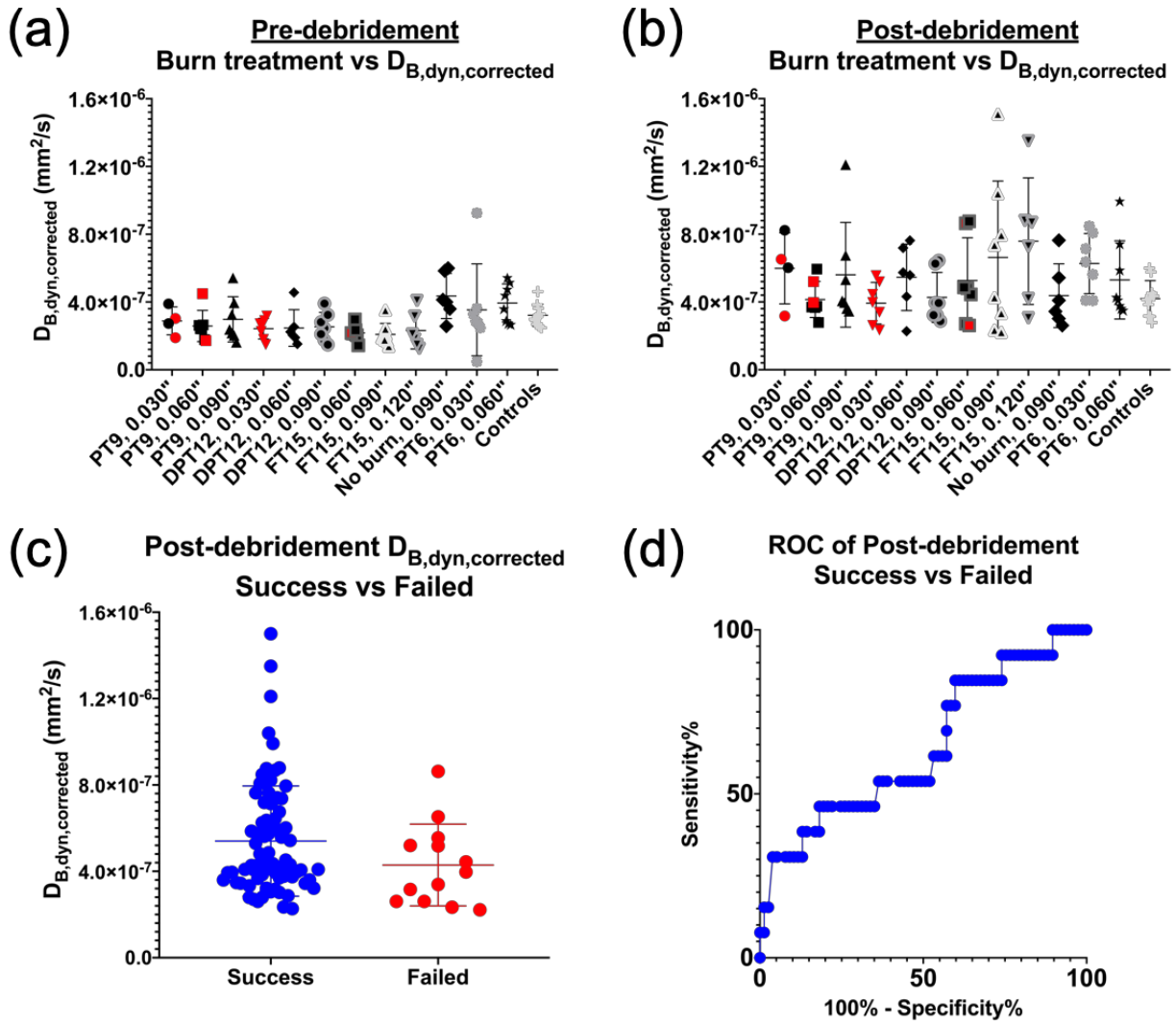

Figure 3.8: Burn treatment vs $D_{B,dyn,corrected}$ and resulting ROC curve. (a) Pre-debridement $D_{B,dyn,corrected}$ displays decreasing mean values with increasing burn severity. (b) Post-debridement $D_{B,dyn,corrected}$ shows overall increased values compared to pre-debridement (mean percent increase of 115% compared to pre-debridement). (c) Mean percent error at post-debridement from pre-debridement for successful and failed grafts were 121% and 76%. (d) The ROC curve showed poor sensitivity and specificity with specificity of 40% when sensitivity was 85%.

3.5. Discussion and Conclusion

LSI can provide meaningful blood flow information in assessing burn wound severity[15,16,19,30,37,60–62]. However, since burn wounds are dynamically changing in the first 48-72 hours post-burn, optical properties are constantly changing during this time point as well[16,63]. Here, we have shown the potential errors associated with assuming optical

properties and how they affect measured blood flow. If the assumed μ_s' is less than the measured μ_s', which occurred at all time points in this study, $D_{B,dyn,corrected}$ will be less than $D_{B,uncorrected}$. This is due to the increase in scattering that would lead to a higher SFI value at the same D_B value, so D_B must actually be a lower value in order to represent the same measured SFI value if μ_s' is greater. If assumed μ_a is greater than measured μ_a, $D_{B,dyn,corrected}$ will be greater to achieve the same SFI value. This is due to the reduction in SFI as absorption increases, so the value of D_B must increase in order to achieve the same SFI value. A plot of varying optical properties and their effect on the SFI vs D_B relationship can be found in the Appendix.

In the case where μ_s' and μ_a were assumed (μ_s'=1mm^{-1}, μ_a=0.01mm^{-1}), we observed mean percent errors up to 47.6% from $D_{B,dyn,corrected}$ (occurred at pre-burn). An explanation was the greater actual μ_s' and lower actual μ_a at pre-burn (μ_s'=1.34mm^{-1}, μ_a=0.0043mm^{-1}). If μ_s' and μ_a are used from the pre-burn time point and assumed to remain constant at post-burn and pre- and post-debridement, we observed mean percent errors up to 19.6% (occurred at post-debridement). At post-debridement, μ_a increased to 0.0097mm^{-}1 from 0.0043mm^{-1} at pre-burn, which resulted in an increase in $D_{B,dyn,corrected}$ associated with the same SFI value. Therefore, continually measuring optical properties plays an important role in obtaining more accurate values of blood flow using LSI.

In comparing $D_{B,dyn,corrected}$ against burn treatments at post-debridement, we were unable to obtain a threshold value for $D_{B,dyn,corrected}$ that would lead to high sensitivity and high specificity for distinguishing burn wounds that were not adequately debrided. However, we believe that by using a single or double normalization to account for local and global changes in blood flow, respectively, we may be able to determine a threshold value

for $D_{B,dyn,corrected}$. Additional failed graft sites from future experiments and their associated $D_{B,dyn,corrected}$ values should improve our sensitivity and specificity.

Although we have shown that we can quantify the errors associated with assuming or not properly correcting for optical property changes, there are limitations to our study. First, we did not include superficial burn and superficial partial burn wounds in our study. Having the full spectrum of burn severities would provide us with a greater understanding of how $D_{B,dyn,corrected}$ changes over the course of wound healing. By debriding the burn wounds, we disturbed wound healing progression as well. Future studies will monitor changes in $D_{B,dyn,corrected}$ longitudinally without debridement. Second, we used μ_s' interpolated at 808nm to match the wavelength used in our LSI system. However, we are aware that SFDI penetrates depths of ~5mm[35], whereas LSI has penetration depths are <1mm. Therefore, the μ_s' of shorter wavelengths may interrogate comparable tissue depths, but the amount of scattering and absorption of chromophores at these shorter wavelengths may not be representative of the 808nm wavelength.

In summary, LSI and SFDI are both promising optical techniques capable of providing clinicians with quantitative and objective measurements of burn wound severity. We were able to quantify the potential errors associated with assuming optical properties and not properly accounting for optical property changes in dynamic burn wounds. By pairing LSI with SFDI, we can reduce inaccuracies in blood flow measurements by properly accounting for the changing optical properties in burn wounds.

3.6 Acknowledgement

This material is based upon work supported by the Air Force Office of Scientific Research under award numbers FA9550-17-1-0193, FA9550-14-1-0034, and FA9550-16-1-0342, which funded development of the LSI technology at the Beckman Laser Institute and the imaging of the 5cm burns and skin grafts at the Institute of Surgical Research . We also acknowledge support from the Arnold and Mabel Beckman Foundation, the NIH Laser Microbeam and Medical Program Grant P41 EB015890, and the NIH funded Institute of Clinical and Translational Science TL1 TR001415 Fellowship to Ben Lertsakdadet. This research was also supported in part by an appointment of Gordon T. Kennedy to the Postgraduate Research Participation Program at the U.S. Army Institute of Surgical Research administered by the Oak Ridge Institute for Science and Education through an interagency agreement between the U.S. Department of Energy and USAISR. The content is solely the responsibility of the authors and does not necessarily represent the official views of the NIGMS, NIBIB or NIH. Any opinions, finding, and conclusions or recommendations expressed in this material are those of the authors and do not necessarily reflect the views of the United States Air Force. We would like to thank the staff and technicians at the Institute of Surgical Research and the Wide-field Functional Imaging Lab members and Microvascular Therapeutics and Imaging Lab members for their support and invaluable feedback.

CHAPTER 4: Summary and Conclusion

We originally set out to address the issue of intestinal failure (IF) monitoring in premature neonates in the neonatal intensive care unit (NICU). Our proposed method was to apply a non-invasive optical imaging modality to objectively quantify and monitor blood flow changes in the abdominal region of these premature neonates. Laser Speckle Imaging (LSI) was our choice modality for this task. Since LSI systems are highly sensitive to motion, most LSI studies are typically performed using mounted systems. However, in order to make LSI more accessible for a NICU, and clinical use in general, we first needed to explore alternative form factors of the LSI device.

Our first goal was to identify a suitable form factor for ease-of-use and ease-of-transportation. Our proposed solution was a handheld LSI device. We made significant modifications to our previous handheld LSI device by incorporating more modular components and increasing the field of view (FOV) to sample larger areas. However, motion artifact remained a concern for using LSI in a handheld configuration. We incorporated a FM into our imaging protocol to sort images based on motion artifact and to identify "useable" images, which had a speckle contrast (K) of the FM above a predefined threshold value. We then aligned these images using the FM as a reference for co-registration. We automated the process of FM identification, sorting images based on K_{FM}, and co-registering useable frames. We showed that our handheld LSI device with our FM imaging protocol could provide comparable results to a mounted LSI device.

Next, we wanted to see if we can further reduce the motion artifact in handheld LSI measurements. So we incorporated a handheld gimbal stabilizer (HGS) to the handheld LSI device, which we called the Motion Stabilized LSI (msLSI) device. Adding a HGS to a LSI

device provided additional stabilization when acquiring data in a handheld configuration and was a novel concept that we wanted to test.

In addition to the HGS, we increased the FOV to 140mm x 105mm, to allow for even larger samples to be measured in a single image. We compared the handheld use of our msLSI device with and without the HGS using *in vitro* flow phantom experiments. The msLSI device showed improved K compared to handheld LSI without the HGS at all flow speeds. The mean number of images above the threshold K_{FM} value was also significantly greater when using the msLSI device.

To further test our msLSI device, we reduced the FOV of the msLSI device to 20mm x 15mm to image the vasculature in a dorsal skinfold window chamber model. For these *in vivo* experiments, we also developed an image processing workflow that automated the identification of the window chamber, sorted images based on the mean K of the tissue within the window chamber (K_{WC}) , and aligned all images using the window chamber. In doing so, the tissue within the window chamber acted as the FM for these experiments. Using the msLSI device resulted in a greater number of images above a threshold K_{WC} value compared to handheld LSI without the HGS. We wanted to compare the signal-to-background ratio (SBR) of the average SFI images that resulted from the msLSI and handheld without HGS data sets. The signal was determined from the SFI value from the vessels and the background was determined from the SFI value from the background tissue. Less motion artifact is associated with higher SBR, and msLSI data resulted in higher SBR compared to handheld without HGS. We were able to show that by pairing a HGS with handheld LSI, we could further reduce motion artifact in handheld LSI data acquisition.

Lastly, in addition to motion artifact concerns for LSI imaging, optical property changes in dynamic wounds can also lead to inaccuracies in measured blood flow. This is an issue for currently commercialized, mounted LSI devices as well.

An example of a dynamic wound model is a burn wound. LSI has been utilized for measuring blood flow in burn wounds for assessing burn severity[15,16,55,60,61]. However, burn wounds are highly dynamic wounds making them a relevant model for comparing the effects of optical property changes on actual blood flow. The dynamic nature of burn wounds within the first 48-72 hours makes them extremely difficult to diagnose accurately[30]. Although studies have shown that blood perfusion is an adequate method for assessing burn wounds, they do not consider the structural changes that occur[55]. A non-contact imaging modality capable of quantifying these structural changes is Spatial Frequency Domain Imaging (SFDI), which is an imaging technique that measures optical properties of tissue (reduced scattering coefficient, μ_s', and absorption coefficient , μ_a) along with oxy- and deoxy-hemoglobin information[34–39].

We hypothesized that by utilizing SFDI to determine optical properties of the burn wounds, we can improve the accuracy of the perfusion information measured by LSI. We showed that assuming optical properties or using the optical properties from a single time point can lead to the errors up to 47% between the measured blood flow to the actual characteristic diffusion coefficient (D_B) value associated with the imaged tissue.

Collectively, this work demonstrates our attempts at providing a viable alternative for clinical blood flow imaging with our handheld LSI device and imaging protocol and the importance of properly accounting for motion artifact and optical property changes in LSI.

With these considerations, a msLSI device may be suitable for clinical use to assist physicians in assessing patients in the neonatal intensive care unit (NICU) and burn unit.

REFERENCES

1. Khan, F. a. *et al.* Predictors of Enteral Autonomy in Children with Intestinal Failure: A Multicenter Cohort Study. *J. Pediatr.* (2015). doi:10.1016/j.jpeds.2015.03.040
2. Squires, R. H. *et al.* Natural History of Pediatric Intestinal Failure: Initial Report from the Pediatric Intestinal Failure Consortium. *J. Pediatr.* **161,** 723–728.e2 (2012).
3. Pittman, R. in *Regulation of Tissue Oxygenation* (Sciences, Claypool Life, 2011). at <https://www.ncbi.nlm.nih.gov/books/NBK54112/?report=classic>
4. Lack of research, drug development detrimental to neonatal patients. *Infect. Dis. Child.* at <http://www.healio.com/pediatrics/neonatal-medicine/news/print/infectious-diseases-in-children/%7Ba9e528b9-3de7-49c6-bd4a-879c502b75fe%7D/lack-of-research-drug-development-detrimental-to-neonatal-patients>
5. Briers, J. D. & Webster, S. Laser Speckle Contrast Analysis (LASCA): A nonscanning, full-field technique for monitoring capillary blood flow. *J. Biomed. Opt.* **1,** 174–179 (1996).
6. Boas, D. a & Dunn, A. K. Laser speckle contrast imaging in biomedical optics. *J. Biomed. Opt.* **15,** 011109 (2010).
7. Boas, D. a & Dunn, A. K. Laser speckle contrast imaging in biomedical optics. *J. Biomed. Opt.* **15,** 011109 (2014).
8. Fercher, A. F. & Briers, J. D. Flow visualization by means of single-exposure speckle photography. *Opt. Commun.* **37,** 326–330 (1981).
9. Mandel, L. Intensity correlation time of an optical field. *Opt. Commun.* **36,** 87–89 (1981).

10. Choi, B., Ramirez-san-juan, J. C., Lotfi, J. & Nelson, J. S. Linear response range characterization and in vivo. *J. Biomed. Opt.* **11(4),** 1–7 (2006).
11. Crouzet, C. *et al.* Cerebral blood flow is decoupled from blood pressure and linked to EEG bursting after resuscitation from cardiac arrest. *Biomed. Opt. Express* **7,** 4660 (2016).
12. Moy, A. J. *et al.* Wide-field functional imaging of blood flow and hemoglobin oxygen saturation in the rodent dorsal window chamber. *Microvasc. Res.* **82,** 199–209 (2011).
13. Moy, W. J. *et al.* Preclinical In Vivo Evaluation of Npe6-Mediated Photodynamic Therapy on Normal Vasculature. *Lasers Surg Med* **44,** 158–162 (2012).
14. Kelly, K. M. *et al.* Talaporfin Sodium-Mediated Photodynamic Therapy Alone and in Combination with Pulsed Dye Laser on Cutaneous Vasculature. *J. Invest. Dermatol.* 2–4 (2014). doi:10.1038/jid.2014.304
15. Ponticorvo, A. *et al.* Quantitative assessment of graded burn wounds in a porcine model using spatial frequency domain imaging (SFDI) and laser speckle imaging (LSI). **5,** 36–45 (2014).
16. Ponticorvo, A. *et al.* Quantitative long-term measurements of burns in a rat model using Spatial Frequency Domain Imaging (SFDI) and Laser Speckle Imaging (LSI). *Lasers Surg. Med.* **49,** 293–304 (2017).
17. Katsui, S., Inoue, Ã. Y., Igari, K., Toyofuku, T. & Kudo, T. Novel Assessment Tool Based on Laser Speckle Contrast Imaging to Diagnose Severe Ischemia in the Lower Limb for. 1–7 (2017). doi:10.1002/lsm.22669
18. de M. Matheus, A. S., Clemente, E. L. S., de Lourdes Guimarães Rodrigues, M., Torres

Valença, D. C. & Gomes, M. B. Assessment of microvascular endothelial function in type 1 diabetes using laser speckle contrast imaging. *J. Diabetes Complications* **31,** 753–757 (2017).

19. Mirdell, R., Iredahl, F., Sjöberg, F., Farnebo, S. & Tesselaar, E. Microvascular blood flow in scalds in children and its relation to duration of wound healing: A study using laser speckle contrast imaging. *Burns* **42,** 648–654 (2016).
20. Bray, R. C., Forrester, K. R., Reed, J., Leonard, J. & Tulip, J. Endoscopic Laser Speckle Imaging of Tissue Blood Flow:Applications in the Human Knee. *J. Orthop. Res.* **August,** 1650–1659 (2006).
21. Yang, B. *et al.* Intraoperative, real-time monitoring of blood flow dynamics associated with laser surgery of port wine stain birthmarks. *Lasers Surg. Med.* **47,** 469–475 (2015).
22. Kojima, S. *et al.* Laser Speckle Contrast Imaging for Intraoperative Quantitative Assessment of Intestinal Blood Perfusion During Colorectal Surgery: A Prospective Pilot Study. *Surg. Innov.* 155335061882342 (2019). doi:10.1177/1553350618823426
23. Molnar, E. *et al.* Evaluation of Laser Speckle Contrast Imaging for the Assessment of Oral Mucosal Blood Flow following Periodontal Plastic Surgery: An Exploratory Study. *Biomed Res. Int.* **2017,** (2017).
24. Farraro, R., Fathi, O. & Choi, B. Handheld , point-of-care laser speckle imaging. *J. Biomed. Opt.* **21,** (2016).
25. Rege, A. *et al.* Noninvasive Assessment of Retinal Blood Flow Using a Novel Handheld Laser Speckle Contrast Imager. **7,** (2018).

26. American Burn Association. Burn Injury Fact Sheet. 1–2 (2018). at <http://ameriburn.org/wp-content/uploads/2017/12/nbaw-factsheet_121417-1.pdf>

27. Heimbach, D., Grube, B. & Marvin, J. Burn Depth : A Review. *World* 10–15 (1992).

28. Singh, V., Devgan, L., Bhat, S. & Milner, S. M. The pathogenesis of burn wound conversion. *Ann. Plast. Surg.* **59,** 109–115 (2007).

29. Shupp, J. W. *et al.* A review of the local pathophysiologic bases of burn wound progression. *J. Burn Care Res.* **31,** 849–873 (2010).

30. Ponticorvo, A. *et al.* Evaluating clinical observation versus Spatial Frequency Domain Imaging (SFDI), Laser Speckle Imaging (LSI) and thermal imaging for the assessment of burn depth. *Burns* 1–11 (2018). doi:10.1016/j.burns.2018.09.026

31. Davis, S. C., Mertz, P. M., Bilevich, E. D., Cazzaniga, A. L. & Eaglstein, W. H. Early Debridement of Second-Degree Burn Wounds Enhances the Rate of Epithelization—An Animal Model to Evaluate Burn Wound Therapies. *J. Burn Care Rehabil.* **17,** 558–561 (1996).

32. Eski, M. *et al.* Cerium nitrate treatment prevents progressive tissue necrosis in the zone of stasis following burn. *Burns* **38,** 283–289 (2012).

33. Firat, C. *et al.* β-Glucan treatment prevents progressive burn ischaemia in the zone of stasis and improves burn healing: An experimental study in rats. *Burns* **39,** 105–112 (2013).

34. Cuccia, D. J. Spatial Frequency Domain Imaging (SFDI): a technology overview and validation of an LED-based clinic-friendly device. *SPIE Emerg. Digit. Micromirror Device Based Syst. Appl.* **8254,** 825405 (2012).

35. O'Sullivan, T. D., Cerussi, A. E., Cuccia, D. J. & Tromberg, B. J. Diffuse optical imaging using spatially and temporally modulated light. *J. Biomed. Opt.* **17,** 0713111 (2012).

36. Ghijsen, M. Quantitative real-time optical imaging of the tissue metabolic rate of oxygen consumption. *J. Biomed. Opt.* **23,** 1 (2018).

37. Nguyen, J. Q. *et al.* Spatial frequency domain imaging of burn wounds in a preclinical model of graded burn severity. *J. Biomed. Opt.* **18,** 066010 (2013).

38. Gioux, S. *et al.* Three-Dimensional Surface Profile Intensity Correction for Spatially-Modulated Imaging. *J. Biomed. Opt.* **14,** 034045 (2009).

39. Erickson, T. A., Mazhar, A., Cuccia, D., Durkin, A. J. & Tunnell, J. W. Lookup-table method for imaging optical properties with structured illumination beyond the diffusion theory regime. *J. Biomed. Opt.* **15,** 036013 (2010).

40. Cuccia, D. J., Bevilacqua, F., Durkin, A. J., Ayers, F. R. & Tromberg, B. J. Quantitation and mapping of tissue optical properties using modulated imaging. *J. Biomed. Opt.* **14,** 24012 (2009).

41. White, S. M. *et al.* Imaging to Assess Blood Flow and Oxygenation in Implantable Engineered Tissues. *Tissue Eng. Part C Methods* **18,** 697–709 (2012).

42. Tesselaar, E., Flejmer, A. M., Farnebo, S. & Dasu, A. Changes in skin microcirculation during radiation therapy for breast cancer. *Acta Oncol. (Madr).* **56,** 1072–1080 (2017).

43. Omarjee, L. *et al.* Optimisation of movement detection and artifact removal during laser speckle contrast imaging. *Microvasc. Res.* **97,** 75–80 (2015).

44. Lertsakdadet, B. *et al.* Correcting for motion artifact in handheld laser speckle images. *J. Biomed. Opt.* **23,** (2018).

45. Quantiles. at <https://www.statsdirect.com/help/nonparametric_methods/quantiles.htm>

46. White, S. M., Valdebran, M., Kelly, K. M. & Choi, B. Simultaneous Blood Flow Measurement and Dermoscopy of Skin Lesions Using Dual-Mode Dermascope. *Sci. Rep.* **8,** 16941 (2018).

47. Yang, O. & Choi, B. Laser speckle imaging using a consumer-grade color camera. *Opt. Lett.* **37,** 3957–3959 (2012).

48. Dunn, C. E., Lertsakdadet, B., Crouzet, C., Bahani, A. & Choi, B. Comparison of speckleplethysmographic (SPG) and photoplethysmographic (PPG) imaging by Monte Carlo simulations and in vivo measurements. *Biomed. Opt. Express* **9,** 481–486 (2018).

49. Jaspers, M. E. H., van Haasterecht, L., van Zuijlen, P. P. M. & Mokkink, L. B. A systematic review on the quality of measurement techniques for the assessment of burn wound depth or healing potential. *Burns* (2018). doi:10.1016/j.burns.2018.05.015

50. Nguyen, K., Ward, D., Lam, L. & Holland, A. J. A. Laser Doppler Imaging prediction of burn wound outcome in children: Is it possible before 48 h? *Burns* **36,** 793–798 (2010).

51. Burke-Smith, A., Collier, J. & Jones, I. A comparison of non-invasive imaging modalities: Infrared thermography, spectrophotometric intracutaneous analysis and laser Doppler imaging for the assessment of adult burns. *Burns* **41,** 1695–1707 (2015).

52. RIVA, C., ROSS, B. & BENEDEK, G. B. Laser Doppler Measurements of Blood Flow in

Capillary Tubes and Retinal Arteries. *Invest. Ophthalmol. Vis. Sci.* **11,** 936–944 (1972).

53. Murray, A. K., Herrick, A. L. & King, T. A. Laser Doppler imaging: A developing technique for application in the rheumatic diseases. *Rheumatology* **43,** 1210–1218 (2004).

54. Millet, C., Roustit, M., Blaise, S. & Cracowski, J. L. Comparison between laser speckle contrast imaging and laser Doppler imaging to assess skin blood flow in humans. *Microvasc. Res.* **82,** 147–151 (2011).

55. Mirdell, R., Farnebo, S., Sjöberg, F. & Tesselaar, E. Accuracy of laser speckle contrast imaging in the assessment of pediatric scald wounds. *Burns* **44,** 90–98 (2018).

56. Carlsson, A. H. *et al.* Antecedent thermal injury worsens split-thickness skin graft quality: A clinically relevant porcine model of full-thickness burn, excision and grafting. *Burns* **43,** 223–231 (2017).

57. Mazhar, A. *et al.* Laser speckle imaging in the spatial frequency domain. **2,** 2088–2094 (2011).

58. GraphPad Software, I. Comparing slopes of linear regression lines. (2017). at <https://www.graphpad.com/support/faq/how-does-prism-compare-the-slopes-of-linear-regression-lines-if-there-are-three-or-more-lines-how-can-i-account-for-multiple-comparisons/>

59. GraphPad Software, I. How to test for a significant difference between the slopes of two linear regression lines when the intercepts are fixed? (2009). at <https://www.graphpad.com/support/faq/how-to-test-for-a-significant-difference-between-the-slopes-of-two-linear-regression-lines-iwhen-the-intercepts-are-fixedi/>

60. Ragol, S. *et al.* Static laser speckle contrast analysis for noninvasive burn diagnosis using a camera-phone imager. *J. Biomed. Opt.* **20,** 086009 (2015).

61. Burmeister, D. M. *et al.* Utility of spatial frequency domain imaging (SFDI) and laser speckle imaging (LSI) to non-invasively diagnose burn depth in a porcine model. *Burns* **41,** 1242–1252 (2015).

62. Burmeister, D. M. *et al.* Noninvasive Techniques for the Determination of Burn Severity in Real Time. *J. Burn Care Res.* **38,** 180–191 (2017).

63. Kennedy, G. *et al.* Spatial frequency domain imaging tracks healing following split-thickness skin grafts of burn wounds (Conference Presentation). in 30 (2018). doi:10.1117/12.2290961

Appendix

Table A.1 and A.2 show the μ_s' and μ_a at 808nm before burn treatment is performed. The mean μ_s' and μ_a were 1.34mm^{-1} and 0.0043mm^{-1}, respectively.

Table A.1: Pre-burn $\mu_{s,808}'$ (mm^{-1}) associated with burn treatment

PT9, 0.030"	PT9, 0.060"	PT9, 0.090"	DPT12, 0.030"	DPT12, 0.060"	DPT12, 0.090"	FT15, 0.060"	FT15, 0.090"	FT15, 0.120"	No burn, 0.090"	PT6, 0.030"	PT6, 0.060"	Controls
1.46	1.47	1.50	1.60	1.47	1.47	1.52	1.49	1.48	1.55	1.44	1.51	1.48
1.53	1.60	1.45	1.65	1.65	1.51	1.59	1.55	1.59	1.55	1.66	1.62	1.46
1.53	1.47	1.53	1.54	1.46	1.46	1.58	1.61	1.56	1.54	1.59	1.62	1.53
1.57	1.43	1.45	1.46	1.47	1.50	1.46	1.48	1.54	1.48	1.39	1.67	1.52
	1.57	1.47	1.53	1.55	1.56	1.49	1.47	1.40	1.38	1.62	1.59	1.55
	1.43	1.42	1.61		1.39	1.43	1.39			1.33	1.52	1.44
										1.35	1.39	1.60
											1.35	1.60
												1.39
												1.34

Table A.2: Pre-burn $\mu_{a,808}$ (mm^{-1}) associated with burn treatment

PT9, 0.030"	PT9, 0.060"	PT9, 0.090"	DPT12, 0.030"	DPT12, 0.060"	DPT12, 0.090"	FT15, 0.060"	FT15, 0.090"	FT15, 0.120"	No burn, 0.090"	PT6, 0.030"	PT6, 0.060"	Controls
0.0034	0.0053	0.0062	0.0035	0.0051	0.0060	0.0038	0.0057	0.0050	0.0039	0.0054	0.0051	0.0049
0.0069	0.0047	0.0060	0.0047	0.0049	0.0042	0.0044	0.0050	0.0040	0.0048	0.0056	0.0046	0.0043
0.0030	0.0032	0.0039	0.0037	0.0035	0.0029	0.0052	0.0045	0.0048	0.0044	0.0042	0.0049	0.0037
0.0058	0.0047	0.0071	0.0082	0.0065	0.0069	0.0074	0.0049	0.0036	0.0054	0.0050	0.0058	0.0036
	0.0032	0.0073	0.0032	0.0028	0.0033	0.0069	0.0058	0.0096	0.0039	0.0038	0.0038	0.0034
	0.0047	0.0039	0.0039	0.0000	0.0054	0.0037	0.0051			0.0049	0.0030	0.0054
										0.0045	0.0050	0.0044
											0.0045	0.0064
												0.0032
												0.0046

Table A.3 and A.4 show the μ_s' and μ_a at 808nm at post-burn. The mean μ_s' and μ_a were 1.44mm^{-1} and 0.0056mm^{-1}, respectively.

Table A.3: Post-burn $\mu_{s,808}'$ (mm^{-1}) associated with burn treatment

PT9, 0.030"	PT9, 0.060"	PT9, 0.090"	DPT12, 0.030"	DPT12, 0.060"	DPT12, 0.090"	FT15, 0.060"	FT15, 0.090"	FT15, 0.120"	No burn, 0.090"	PT6, 0.030"	PT6, 0.060"	Controls
1.34	1.49	1.51	1.41	1.53	1.37	1.54	1.34	1.40	1.52	1.44	1.49	1.46
1.48	1.41	1.46	1.45	1.36	1.47	1.35	1.27	1.33	1.58	1.63	1.51	1.44
1.54	1.35	1.43	1.23	1.24	1.24	1.39	1.24	1.30	1.53	1.59	1.63	1.50
1.53	1.50	1.27	1.51	1.41	1.43	1.16	1.23	1.22	1.50	1.49	1.58	1.49
	1.63	1.55	1.57	1.49	1.53	1.34	1.38	1.17	1.42	1.64	1.66	1.62
	1.49	1.62	1.51	1.39	1.43	1.30	1.29	1.17	1.52	1.42	1.64	1.59
	1.43	1.49	1.42		1.41	1.23	1.35			1.51	1.49	1.54
							1.49				1.48	1.31
												1.51
												1.51

Table A.4: Post-burn $\mu_{a,808}$ (mm^{-1}) associated with burn treatment

PT9, 0.030"	PT9, 0.060"	PT9, 0.090"	DPT12, 0.030"	DPT12, 0.060"	DPT12, 0.090"	FT15, 0.060"	FT15, 0.090"	FT15, 0.120"	No burn, 0.090"	PT6, 0.030"	PT6, 0.060"	Controls
0.0050	0.0067	0.0076	0.0045	0.0059	0.0074	0.0051	0.0058	0.0052	0.0042	0.0074	0.0069	0.0046
0.0076	0.0066	0.0073	0.0057	0.0055	0.0050	0.0051	0.0045	0.0049	0.0048	0.0067	0.0067	0.0043
0.0046	0.0045	0.0050	0.0055	0.0045	0.0045	0.0048	0.0043	0.0057	0.0048	0.0058	0.0067	0.0036
0.0060	0.0060	0.0108	0.0095	0.0070	0.0071	0.0098	0.0058	0.0043	0.0054	0.0073	0.0071	0.0041
	0.0055	0.0086	0.0046	0.0046	0.0047	0.0068	0.0061	0.0089	0.0036	0.0059	0.0053	0.0047
	0.0059	0.0049	0.0060	0.0061	0.0062	0.0034	0.0054	0.0039	0.0045	0.0057	0.0054	0.0073
	0.0060	0.0053	0.0053		0.0046	0.0047	0.0047			0.0052	0.0073	0.0043
							0.0036				0.0057	0.0047
												0.0027
												0.0041

Table A.5 and A.6 show the μ_s' and μ_a at 808nm at pre-debridement. The mean μ_s' and μ_a were 1.45mm^{-1} and 0.0093mm^{-1}, respectively.

Table A.5: Pre-debridement $\mu_{s,808}$' (mm^{-1}) associated with burn treatment

PT9, 0.030"	PT9, 0.060"	PT9, 0.090"	DPT12, 0.030"	DPT12, 0.060"	DPT12, 0.090"	FT15, 0.060"	FT15, 0.090"	FT15, 0.120"	No burn, 0.090"	PT6, 0.030"	PT6, 0.060"	Controls
1.40	1.48	1.54	1.25	1.60	1.48	1.47	1.46	1.47	1.45	1.51	1.51	1.55
1.44	1.48	1.22	1.52	1.46	1.21	1.46	1.66	1.47	1.57	1.55	1.35	1.38
1.41	1.44	1.54	1.28	1.40	1.36	1.51	1.54	1.15	1.54	1.44	1.55	1.46
1.57	1.58	1.33	1.62	1.47	1.45	1.30	1.36	1.25	1.56	1.61	1.46	1.42
	1.56	1.61	1.46	1.46	1.56	1.42	1.36	1.45	1.40	1.59	1.29	1.61
	1.48	1.41	1.57	1.36	1.30	1.29	1.42	1.37	1.55	1.07	1.32	1.54
	1.43	1.46	1.50		1.56	1.54	1.35			1.46	1.30	1.42
							1.52				1.35	1.48
												1.50
												1.49

Table A.6: Pre-debridement $\mu_{a,808}$ (mm^{-1}) associated with burn treatment

PT9, 0.030"	PT9, 0.060"	PT9, 0.090"	DPT12, 0.030"	DPT12, 0.060"	DPT12, 0.090"	FT15, 0.060"	FT15, 0.090"	FT15, 0.120"	No burn, 0.090"	PT6, 0.030"	PT6, 0.060"	Controls
0.0093	0.0095	0.0101	0.0139	0.0103	0.0100	0.0095	0.0086	0.0085	0.0047	0.0090	0.0088	0.0038
0.0137	0.0104	0.0122	0.0100	0.0103	0.0138	0.0092	0.0104	0.0098	0.0047	0.0111	0.0132	0.0045
0.0087	0.0081	0.0082	0.0092	0.0102	0.0080	0.0100	0.0092	0.0130	0.0055	0.0103	0.0102	0.0039
0.0114	0.0089	0.0143	0.0114	0.0088	0.0088	0.0142	0.0107	0.0067	0.0041	0.0110	0.0134	0.0046
	0.0102	0.0104	0.0123	0.0096	0.0092	0.0100	0.0074	0.0090	0.0050	0.0084	0.0111	0.0047
	0.0102	0.0115	0.0102	0.0116	0.0128	0.0078	0.0103	0.0072	0.0045	0.0101	0.0092	0.0066
	0.0094	0.0079	0.0083		0.0073	0.0248	0.0072			0.0092	0.0139	0.0036
							0.0073				0.0087	0.0053
												0.0047
												0.0060

Table A.7 and A.8 show the μ_s' and μ_a at 808nm at post-debridement. The mean μ_s' and μ_a were 1.42mm^{-1} and 0.0097mm^{-1}, respectively.

Table A.7: Post-debridement $\mu_{s,808}$' (mm^{-1}) associated with burn treatment

PT9, 0.030"	PT9, 0.060"	PT9, 0.090"	DPT12, 0.030"	DPT12, 0.060"	DPT12, 0.090"	FT15, 0.060"	FT15, 0.090"	FT15, 0.120"	No burn, 0.090"	PT6, 0.030"	PT6, 0.060"	Controls
1.39	1.38	1.43	1.25	1.34	1.44	1.33	1.37	1.30	1.26	1.18	1.37	1.52
1.58	1.35	1.18	1.37	1.19	1.20	1.31	1.34	1.30	1.53	1.41	1.25	1.34
1.15	1.53	1.32	1.42	1.37	1.37	1.41	1.25	1.20	1.48	1.41	1.45	1.47
1.38	1.48	1.42	1.93	1.57	1.64	1.40	1.40	1.36	1.43	1.41	1.17	1.39
	1.43	1.64	1.40	1.40	1.19	1.71	1.61	1.43	1.43	1.29	1.39	1.56
	1.61	1.47	1.45	1.43	1.51	1.45	1.43	1.40	1.48	1.32	1.37	1.48
	1.57	1.51	1.64		1.56	1.55	1.54			1.51	1.48	1.51
							1.58				1.65	1.42
												1.54
												1.33

Table A.8: Post-debridement $\mu_{a,808}$ (mm^{-1}) associated with burn treatment

PT9, 0.030"	PT9, 0.060"	PT9, 0.090"	DPT12, 0.030"	DPT12, 0.060"	DPT12, 0.090"	FT15, 0.060"	FT15, 0.090"	FT15, 0.120"	No burn, 0.090"	PT6, 0.030"	PT6, 0.060"	Controls
0.0079	0.0075	0.0092	0.0109	0.0091	0.0107	0.0079	0.0143	0.0167	0.0112	0.0059	0.0071	0.0033
0.0079	0.0111	0.0094	0.0117	0.0113	0.0116	0.0115	0.0199	0.0170	0.0125	0.0109	0.0127	0.0036
0.0050	0.0064	0.0107	0.0095	0.0094	0.0085	0.0171	0.0174	0.0261	0.0098	0.0105	0.0103	0.0043
0.0138	0.0051	0.0089	0.0079	0.0084	0.0130	0.0118	0.0106	0.0111	0.0073	0.0068	0.0149	0.0045
	0.0083	0.0073	0.0096	0.0080	0.0178	0.0083	0.0087	0.0089	0.0081	0.0065	0.0112	0.0046
	0.0111	0.0117	0.0111	0.0110	0.0144	0.0092	0.0161	0.0087	0.0087	0.0058	0.0079	0.0068
	0.0072	0.0105	0.0084		0.0060	0.0111	0.0087			0.0073	0.0089	0.0027
							0.0069				0.0090	0.0047
												0.0040
												0.0048

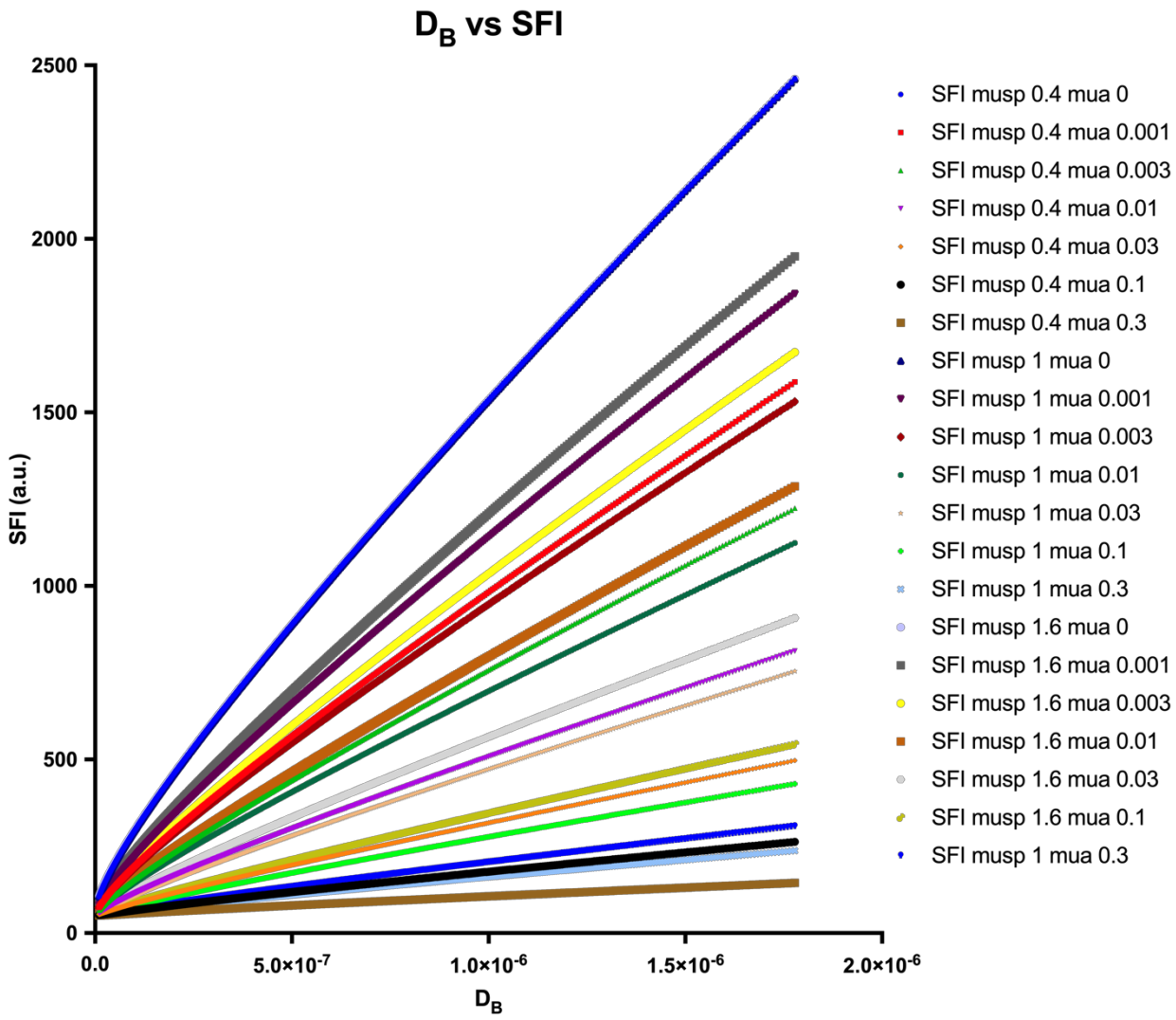

Figure A.1: Varying optical properties and their effects on the SFI vs D_B relationship.